Monthly Notices of the ROYAL ASTRONOMICAL SOCIETY

Mon. Not. R. Astron. Soc. **415,** 2607–2625 (2011) doi:10.1111/j.1365-2966.2011.18884.x

Mismatch and misalignment: dark haloes and satellites of disc galaxies

A. J. Deason,[1★] I. G. McCarthy,[1,2,3] A. S. Font,[1] N. W. Evans,[1] C. S. Frenk,[4] V. Belokurov,[1] N. I. Libeskind,[5] R. A. Crain[6] and T. Theuns[4,7]

[1] *Institute of Astronomy, Madingley Road, Cambridge CB3 0HA*
[2] *Kavli Institute for Cosmology, University of Cambridge, Madingley Road, Cambridge CB3 OHA*
[3] *Astrophysics Group, Cavendish Laboratory, JJ Thomson Avenue, Cambridge CB3 0HE*
[4] *Institute for Computational Cosmology, Department of Physics, University of Durham, South Road, Durham DH1 3LE*
[5] *Astrophysikalisches Institut Potsdam, An der Sternwarte 16, D-14482 Potsdam, Germany*
[6] *Centre for Astrophysics and Supercomputing, Swinburne University of Technology, Hawthorn, Victoria 3122, Australia*
[7] *Department of Physics, University of Antwerp, Campus Groenenborger, Groenenborgerlaan 171, B-2020 Antwerp, Belgium*

Accepted 2011 April 8. Received 2011 March 24; in original form 2010 December 15

ABSTRACT

We study the phase-space distribution of satellite galaxies associated with late-type galaxies in the GIMIC suite of simulations. GIMIC consists of resimulations of five cosmologically representative regions from the Millennium Simulation, which have higher resolution and incorporate baryonic physics. Whilst the disc of the galaxy is well aligned with the inner regions ($r \sim 0.1 r_{200}$) of the dark matter halo, both in shape and angular momentum, there can be substantial misalignments at larger radii ($r \sim r_{200}$). Misalignments of $>45^{\circ}$ are seen in $\sim$30 per cent of our sample. We find that the satellite population aligns with the shape (and angular momentum) of the outer dark matter halo. However, the alignment with the galaxy is weak owing to the mismatch between the disc and dark matter halo. Roughly 20 per cent of the satellite systems with 10 bright galaxies within r_{200} exhibit a polar spatial alignment with respect to the galaxy – an orientation reminiscent of the classical satellites of the Milky Way. We find that a small fraction ($\sim$10 per cent) of satellite systems show evidence for rotational support which we attribute to group infall. There is a bias towards satellites on prograde orbits relative to the spin of the dark matter halo (and to a lesser extent with the angular momentum of the disc). This preference towards co-rotation is stronger in the inner regions of the halo where the most massive satellites accreted at relatively early times are located.

We attribute the anisotropic spatial distribution and angular momentum bias of the satellites at $z = 0$ to their directional accretion along the major axes of the dark matter halo. The satellite galaxies have been accreted relatively recently compared to the dark matter mass and have experienced less phase-mixing and relaxation – the memory of their accretion history can remain intact to $z = 0$. Understanding the phase-space distribution of the $z = 0$ satellite population is key for studies that estimate the host halo mass from the line-of-sight velocities and projected positions of satellite galaxies. We quantify the effects of such systematics in estimates of the host halo mass from the satellite population.

Key words: galaxies: general – galaxies: haloes – galaxies: kinematics and dynamics – cosmology: theory – dark matter.

1 INTRODUCTION

Studies of local galaxies, such as the Milky Way and M31, can potentially provide us with the missing link between cosmological structure formation and the complex baryonic processes that help shape the galaxies we observe today. Any acceptable cosmological model must, in addition to satisfying the requirements of large-scale structure, account for the small-scale detail exhibited by our own Milky Way galaxy and others.

For some time it has been known that the 11 classical satellites of the Milky Way define a highly inclined plane relative to the disc of the Galaxy (Lynden-Bell 1976). Early work by Holmberg (1969) and Zaritsky et al. (1997) found similar alignments in

★E-mail: ajd75@ast.cam.ac.uk

external galaxies whereby the satellites tend to avoid the equatorial regions of the parent light distribution. However, more recent work using the 2df Galaxy Redshift Survey and the Sloan Digital Sky Survey (SDSS) find that the opposite trend is true; satellites tend to avoid the polar regions of the light distribution (Sales & Lambas 2004; Brainerd 2005; Yang et al. 2006). Agustsson & Brainerd (2010) find that the spatial orientation of satellite galaxies depends on the type of host galaxy; satellites of red galaxies are found preferentially near the major axes of their hosts, while satellites of blue galaxies show little or no spatial anisotropy. The anisotropic nature of the spatial distribution of satellite galaxies has led some authors to postulate a discrepancy between observational constraints and models adopting the Λ cold dark matter (ΛCDM) framework (e.g. Kroupa, Theis & Boily 2005). However, numerical studies have shown that preferential alignments are naturally produced in the simulations (Kang et al. 2005; Libeskind et al. 2005; Zentner et al. 2005). The satellites tend to align with the major axis of the dark matter halo, but an extrapolation to the relation with the light distribution is not straightforward in models which do not follow the evolution of baryonic matter.

The radial velocities and available proper motions of the classical Milky Way satellites hint at the presence of coherent motion (Lynden-Bell & Lynden-Bell 1995; Metz, Kroupa & Libeskind 2008). In fact, Metz et al. (2008) find that at least three of the classical satellites have orbital poles aligned (within 30°) with the normal of their spatially defined plane. They suggested that the classical satellites may occupy a rotationally supported disc. Li & Helmi (2008) found that coherence in the motions of the satellites may be due to group infall, whereby satellites fall into the parent halo together and preserve their common motion to the present day. A scenario whereby satellite accretion is along surrounding filamentary structures suggests a link between the angular momentum orientation of the satellite galaxies and the host halo itself (Libeskind et al. 2005; Lovell et al. 2011). A correlation between the orbital motion of satellite galaxies and the spin of their parent light distribution was seen by Azzaro et al. (2006) in a carefully selected sample of SDSS galaxies. However, this bias towards co-rotation was not seen by Hwang & Park (2010) in a larger sample of SDSS host galaxies. The authors find equal numbers of satellites in prograde and retrograde orbits. Numerical simulation studies by Warnick & Knebe (2006) and Shaw et al. (2006) find a bias towards satellites on co-rotating orbits relative to the net spin of their host halo. However, both of these studies base their conclusions on results derived from dark matter only simulations, and they focus on cluster-sized haloes. Observational estimates are frustrated by uncertainties regarding the spin direction of the parent galaxies and contamination by interlopers. On the other hand, theoretical work has solely focused on dark matter only simulations – the orientation of the satellites' orbit with respect to the *stellar* distribution is yet to be tested.

Dark matter only simulations have been hugely influential in developing our knowledge of the large-scale structure of the Universe. However, some of the potential shortcomings of the standard model posed by observations of our own Milky Way galaxy are difficult to reconcile within a simulation that does not include luminous matter. Previous work has made use of semi-analytic models in order to include the necessary baryonic processes into these cosmological simulations (e.g. White & Frenk 1991; Cole et al. 1994; Somerville & Primack 1999; Baugh 2006). Whilst these methods have provided valuable insights into the effects of baryonic physics on galaxy formation, their limited spatial information makes them unsuitable to investigate the processes of interest in this paper. For example, a key assumption in these semi-analytic methods is that the angular momentum of the disc is aligned with the spin of the dark matter halo.

In recent years, increasingly realistic implementations of the hydrodynamic evolution of the baryons have become possible within the framework of cosmological simulations which are able to match a series of galaxy properties and scaling relations (e.g. Gnedin et al. 2004; Governato et al. 2007; Agertz, Teyssier & Moore 2009; Crain et al. 2009; Crain et al. 2010; Font et al. 2011). In particular, these hydrodynamic cosmological simulations are able to follow the changes in shapes and angular momenta of the dark matter and baryons self-consistently. In this paper, we make use of the GIMIC suite of simulations described in detail by Crain et al. (2009). This is a resimulation of five cosmologically representative regions ($\sim 20\,h^{-1}$ Mpc in radius) from the Millennium Simulation (Springel et al. 2005). In these regions, GIMIC incorporates baryonic physics and achieves higher resolution than the Millennium Simulation as a whole.

We use these simulations to study the orbital properties of satellite galaxies in late-type galaxies. In contrast to previous work, we probe the dynamics of the satellites relative to their host's stellar component as well as the unseen dark matter component. In Section 2, we describe the GIMIC suite of simulations in more detail and outline the selection criteria for our sample of parent haloes. In Section 3, we discuss the relation between the galaxy and the dark matter halo in both spatial and velocity space. Section 4 focuses on the satellite galaxies associated with our sample of haloes. We investigate their spatial and angular momentum distribution relative to both the galaxy and dark matter halo. In Section 5, we briefly outline an application of our results to test estimators of the parent halo mass. Finally, in Section 6 we draw our main conclusions.

2 THE NUMERICAL SIMULATIONS

In this section, we briefly describe the simulations we have used and outline our methods for selecting parent galaxy haloes and their associated satellite galaxies.

2.1 GIMIC

The Galaxies-Intergalactic Medium Interaction Calculation (GIMIC) suite of simulations is described in detail in Crain et al. (2009) (see also Crain et al. 2010). It consists of a set of hydrodynamical resimulations of five nearly spherical regions ($\sim 20\,h^{-1}$ Mpc in radius) extracted from the Millennium Simulation (Springel et al. 2005). The regions were selected to have overdensities at $z = 1.5$ that represent $(+2, +1, 0, -1, -2)\sigma$, where σ is the rms deviation from the mean on this spatial scale. The five spheres therefore encompass a wide range of large-scale environments. In the present study, we select systems with total 'main halo' (i.e. the dominant subhalo in a friends-of-friends group) masses similar to that of the Milky Way, irrespective of the environment. Crain et al. (2009) found that the properties of systems of fixed main halo mass do not depend significantly on the large-scale environment (see e.g. fig. 8 of that paper).

We present only a brief summary of the GIMIC simulations here, and refer to Crain et al. (2009, 2010) for more detailed descriptions. The cosmological parameters are the same as those in the Millennium Simulation and correspond to a ΛCDM model with $\Omega_{\rm m} = 0.25$, $\Omega_\Lambda = 0.75$, $\Omega_{\rm b} = 0.045$, $\sigma_8 = 0.9$ (where σ_8 is the rms amplitude of linear mass fluctuations on $8\,h^{-1}$ Mpc scale at $z = 0$), $H_0 = 100\,h\,{\rm km\,s^{-1}\,Mpc^{-1}}$, $h = 0.73$, $n_{\rm s} = 1$ (where $n_{\rm s}$ is the spectral index of the primordial power spectrum).

The simulations were evolved to $z = 0$ using the TreePM-SPH code GADGET, described in Springel (2005). Subsequently, the GADGET code has been substantially modified to incorporate baryonic physics which includes:

(i) a prescription for star formation outlined in Schaye & Dalla Vecchia (2008) that is designed to reproduce the observed Kennicutt–Schmidt law (Kennicutt 1998);

(ii) radiative gas cooling in the presence of a UV/X-ray background (see Haardt & Madau 2001) which includes the contribution of metal-line cooling (computed element-by-element; Wiersma, Schaye & Smith 2009a);

(iii) the timed release of 11 individual metals by both massive [Type II supernovae (SNe) and stellar winds] and intermediate-mass stars (Type Ia SNe and asymptotic giant branch stars; Wiersma et al. 2009b);

(iv) a kinetic SN feedback model (Dalla Vecchia & Schaye 2008) which can quench star formation in low-mass haloes and pollute the Intergalactic Medium (IGM) with metals.

In the present study, we analyse the 'intermediate' resolution GIMIC simulations which have eight times better mass resolution than the Millennium Simulation. These runs have a dark matter particle mass of $M_{\rm dm} \sim 5.30 \times 10^7\,h^{-1}\,{\rm M}_{\odot}$ and an initial gas particle mass of $M_{\rm g} = 1.16 \times 10^7\,h^{-1}\,{\rm M}_{\odot}$. This implies that it is possible to resolve systems with masses similar to that of the classical dwarf galaxies. The remainder of the $500(h^{-1}\,{\rm Mpc})^3$ Millennium volume is modelled with dark matter particles at much lower resolution to ensure that the presence of surrounding large-scale structure is accurately accounted for. Dark matter only runs of the GIMIC simulations are also available (at the same resolution) which can be directly compared to the hydrodynamic versions of the simulations. The -2σ volume of the 'high' resolution GIMIC simulations has also been carried out to redshift $z = 0$. This higher resolution run has eight times better mass resolution than the intermediate runs (and 64 times better than the Millennium Simulation). We check that the conclusions of this paper are not subject to resolution effects by ensuring our main results are unchanged in the higher resolution simulations (see Appendix A).

Previous work utilizing the GIMIC simulations has found encouraging agreement with observational studies. The adopted star formation and feedback prescription results in a good match to the star formation rate history of the universe (Crain et al. 2009; see also Schaye et al. 2010), and also reproduces a number of X-ray/optical scaling relations for normal disc galaxies (Crain et al. 2010). Font et al. (2011) find that the stellar haloes of their simulated Milky Way mass galaxies have luminosities and radial density profiles in good agreement with observations. Furthermore, McCarthy et al. (in preparation) show that the simulated L^* disc galaxies in GIMIC have realistic kinematics and sizes.

2.2 Identification of galaxies and satellites

Bound haloes are identified using the SUBFIND algorithm of Dolag et al. (2009), which extends the standard implementation of Springel et al. (2001) by also including baryonic particles when identifying self-bound substructures. The main galaxy or parent halo is the most massive subhalo belonging to a friends-of-friends system. The other self-bound substructures of the system are then classified as satellite galaxies.

We define r_{200} as the radius at which the mean enclosed density falls to 200 times the critical density ($200\rho_{\rm crit}$). We select parent haloes with total mass within this radius in the range $5 \times 10^{11} < M_{200}/{\rm M}_{\odot} < 5 \times 10^{12}$. Only haloes with at least one associated satellite galaxy (or subhalo) other than the main halo are included. GIMIC is a resimulation and is thus subject to edge effects at the boundaries of the selected spherical regions. We discard any haloes located at the boundary edges that are partially comprised of low-resolution dark matter particles.

We select our sample of parent haloes according to the 'relaxation' criteria defined below, following the same reasoning as Neto et al. (2007).

(1) *Virial ratio*. We compute the ratio $2K/|U|$, where K and U are the total kinetic energy and total potential energy within r_{200}. We adopt $2K/|U| < 1.35$ for the relaxed sample.

(2) *Centre of mass displacement*. The offset between the centre of mass of the halo and position of the most bound particle (potential centre) can be described by the normalized offset parameter, $\epsilon = |r_{\rm c} - r_{\rm cm}|/r_{200}$ (Thomas et al. 2001). Relaxed haloes have $\epsilon < 0.07$.

(3) *Mass in substructure*. For a halo to be considered relaxed, we require the fraction of mass in substructure within r_{200} to be $f_{\rm sub} < 0.1$ and the most massive satellite within $2r_{200}$ to satisfy $M_{\rm sat}/M_{200} < 0.1$.

Under these criteria, approximately 20 per cent of the haloes are unrelaxed (cf. Neto et al. 2007). There are a total of 624 relaxed haloes within the given mass range. Most unrelaxed haloes are recognized from the second and third constraints, whilst only a few haloes are out of virial equilibrium. Note that since only a relatively small fraction of haloes are unrelaxed our conclusions are generally valid.

The galaxies are assigned a morphological classification (i.e. disc and spheroid-dominated types) based on their dynamics. A simple two-component model is assumed: (i) a dispersion-supported spheroid and (ii) a rotationally supported disc. Details of this decomposition into morphological types are given in Crain et al. (2010). Fig. 1 in Crain et al. (2010) shows the distribution of the disc-to-total stellar mass ratios (D/T). In this work, we restrict our sample to late-type galaxies and exclude obviously 'elliptical' galaxies. Following the reasoning of Crain et al. (2010), we adopt a threshold of $D/T > 0.3$. We have checked that our main results are unchanged if other cuts of D/T are imposed (e.g. $D/T > 0.2$ or $D/T > 0.4$). We note that haloes are selected based only on mass and D/T. This selection was not chosen to reproduce Milky Way (or M31) galaxy replicas and comparison with these two Local Group galaxies is made in the broadest sense.

Our final sample of haloes consists of 431 parent haloes and 4864 associated satellite galaxies. We summarize the properties of our sample in Table 1. The approximate (total) mass range of our sample of satellite galaxies is $10^8 < M_{\rm sat} < 10^{11}\,{\rm M}_{\odot}$. Previous work using low-resolution dark matter only simulations have much larger samples of parent haloes (e.g. Sales et al. 2007, who use thousands of parent haloes from the Millennium Simulation). However, our sample size compares favourably to more recent hydrodynamical simulations (e.g. Libeskind et al. 2007, who had only nine parent haloes).

In addition to our hydrodynamical suite of GIMIC simulations, we have also the dark matter only runs. We can match our sample of haloes with their dark matter only counterpart. For each halo, we consider dark matter only haloes with similar masses inside r_{200} (within a factor of 2). We then compute the distances between the positions of the dark matter only haloes and the position of the halo in question. The dark matter only counterpart is then the closest (in position) to the baryonic simulations version of the halo which also has a similar mass.

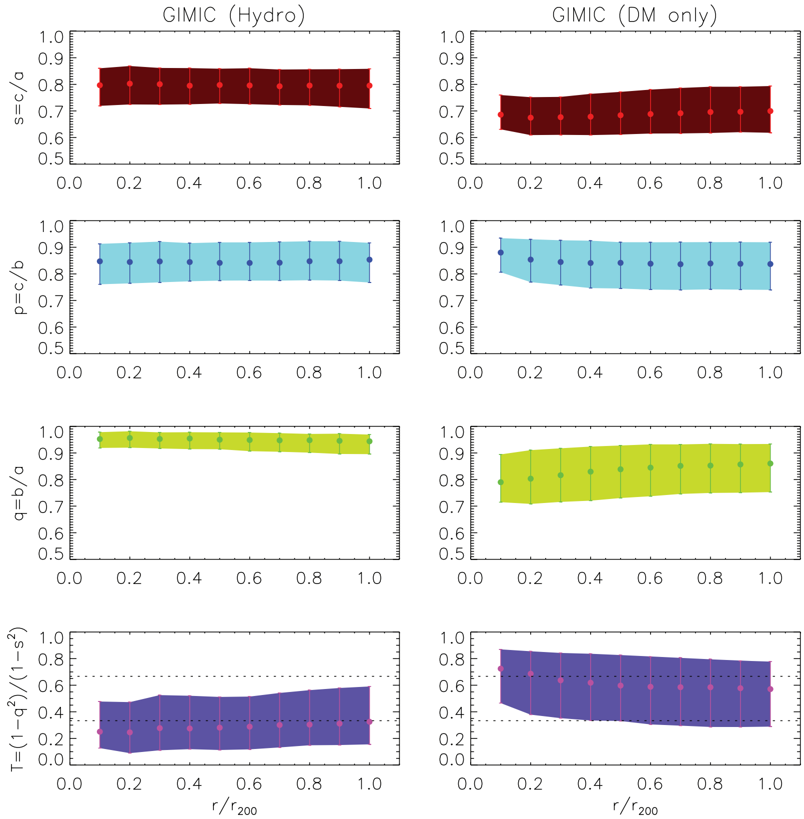

Figure 1. The radial dependence of the axial ratios $s = c/a$ (top panels), $p = c/b$ (second row), $q = b/a$ (third row) and the triaxiality parameter $T = (1 - q^2)/(1 - s^2)$ (bottom panels). The shaded regions show the range of values covered by 68 per cent of the distribution and the points give the median values. The dotted lines indicate the regions of oblate ($T < 1/3$), triaxial ($1/3 < T < 2/3$) and prolate haloes ($T > 2/3$). The right-hand panels are for the dark matter only counterparts of our sample. The halo shapes are rounder (and more oblate) in the hydro GIMIC simulations.

Table 1. The average properties of our sample of (431) galaxy haloes. We give the median halo radius (r_{200}), the median total mass inside this radius (M_{200}), the median parent halo stellar mass ($M_\star$), the median D/T and the median number of satellite galaxies per parent halo ($N_{\rm sat}$).

$\langle r_{200}\rangle$ (kpc)	$\langle M_{200}\rangle$ ($10^{12}\,{\rm M}_\odot$)	$\langle M_\star\rangle$ ($10^{10}\,{\rm M}_\odot$)	$\langle D/T\rangle$	$\langle N_{\rm sat}\rangle$
224	1.4	8.0	0.7	9

3 HALO PROPERTIES

Here, we examine the shapes, the angular momenta and the misalignments of the dark matter haloes of our simulated galaxies.

3.1 Shapes

Haloes are modelled as ellipsoids characterized by three axes, a, b, c, where $a \geq b \geq c$. The axial ratios $s = c/a$, $q = b/a$ and $p = c/b$ describe the three classes of ellipsoids: prolate ($a > b \approx c$), oblate ($a \approx b > c$) and triaxial ($a > b > c$). The shapes of dark matter haloes are computed using the weighted (or reduced) second moment tensor:

$$I_{ij} = \sum_{n=1}^{N(\leq r)} \frac{x_{i,n} x_{j,n}}{r_n^2}, \quad (1)$$

where

$$r_n = \sqrt{x_{1,n}^2 + \frac{x_{2,n}^2}{q^2} + \frac{x_{3,n}^2}{s^2}}. \quad (2)$$

The advantage of this scheme is that every particle is given equal weight, independent of radius. The orientation is defined by the eigenvectors of the second moment tensor. The principal components of the tensor give the axial ratios:

$$q = \sqrt{\frac{I_{yy}}{I_{xx}}}, \quad s = \sqrt{\frac{I_{zz}}{I_{xx}}}. \quad (3)$$

As the value of the elliptical radius, r_n, is not known in advance (it depends on s and q), the axial ratios are computed using an iterative algorithm (Dubinski & Carlberg 1991). In Fig. 1, we show the radial dependence of the three axis ratios. The bottom panel gives the radial behaviour of the triaxiality parameter (Franx, Illingworth & de Zeeuw 1991) defined by

$$T = \frac{1 - (b/a)^2}{1 - (c/a)^2} = \frac{1 - q^2}{1 - s^2}. \quad (4)$$

Oblate, triaxial and prolate haloes have triaxiality parameters of $T < 1/3$, $1/3 < T < 2/3$ and $T > 2/3$, respectively. The right-hand panels of Fig. 1 give the axis ratios for the dark matter only counterparts of our sample. The shaded regions show the values covered by 68 per cent of the distribution and the points denote the median values.

The dark matter haloes in our sample are close to spherical and are slightly more oblate in the inner regions. This is in stark contrast to the haloes in the dark matter only simulations which become more prolate towards the centre. The inclusion of baryonic physics affects the shape of the halo substantially in the inner regions, but also has a significant effect throughout the halo.

Our results broadly agree with the findings of previous studies but direct comparisons are difficult as many authors have concentrated on cluster-sized haloes or have used simulations where the assembly of the central galaxy is not modelled self-consistently. Dubinski (1994), for example, simulates dissipative infall by growing a central mass concentration inside a triaxial dark matter halo and finds that a steeper potential leads to rounder and more oblate dark matter halo shapes [$\Delta(c/a) \sim 0.1$]. Kazantzidis et al. (2004) study cluster-sized haloes using gas dynamical simulations and find they are significantly rounder in the inner regions [$\Delta(c/a) \sim 0.2$] but the changes are radially dependent and are almost negligible at the virial radius. Abadi et al. (2010) employ galaxy models which include radiative gas cooling but neglect the contribution from stellar feedback. They compute equipotential axial ratios and find roughly constant flattening of $\langle c/a \rangle \sim 0.85$, which is significantly rounder than their dark matter only runs. By contrast, we have characterized the halo shape by the density of the dark matter, which is always flatter than the equipotential surfaces. Compared to Abadi et al. (2010), we do not find such a significant change in sphericity relative to the dark matter only simulations. This is presumably because the GIMIC simulations include stellar feedback and do not suffer from strong overcooling (see e.g. Duffy et al. 2010). As indicated in Table 1, the mean stellar mass fraction of our simulated disc galaxies is $\sim$0.057. This corresponds to a baryon conversion efficiency ($M_*/M_{\rm halo} \times \Omega_{\rm m}/\Omega_{\rm b}$) of $\approx$30 per cent, which is only a factor of $\sim$1.5 larger than that inferred recently by Guo et al. (2010) by matching the observed stellar mass function from the most recent SDSS data release to the halo mass function derived from the Millennium and Millennium-II Simulations.

Unfortunately, the evidence on the shape of the Milky Way's dark halo is far from being clear-cut. Many authors have argued that the coherence of the Sagittarius tidal stream may constrain the halo shape. However, this line of enquiry has concluded that the halo may be almost spherical (Ibata et al. 2001; Fellhauer et al. 2006), oblate (Johnston, Law & Majewski 2005), prolate (Helmi 2004) or triaxial (Law & Majewski 2010). This variety of results strongly suggests that halo shape is not the primary factor determining the complex morphology of the Sagittarius stream. Smith et al. (2009) argued that the spherical alignment of the velocity ellipsoid of SDSS halo subdwarf stars implied that the gravitational potential and hence the dark halo was nearly spherical. There is, however, contradictory evidence from studies of the flaring of the H I gas layer by Olling & Merrifield (2000), who found a highly flattened oblate ($q \approx 0.3$) dark halo for the Milky Way.

The dark matter halo shapes of external galaxies are often estimated using galaxy–galaxy weak lensing studies. Hoekstra, Yee & Gladders (2004) and Parker et al. (2007) both found an average axial ratio of $\sim$0.7 from their studies using the Red-Sequence Cluster Survey and the Canada–France–Hawaii Telescope legacy survey, respectively. However, Mandelbaum et al. (2006) found no evidence for halo ellipticity in their study using SDSS data.

3.2 Angular momentum and shape

The (cumulative) specific angular momentum vectors for the dark matter particles, $\boldsymbol{j}_{\rm dm}$, and the stellar component, $\boldsymbol{j}_{\rm gal}$, are defined as

$$\boldsymbol{j}(\leq r) = \frac{1}{M(\leq r)} \sum_{n=1}^{N(\leq r)} m_n \boldsymbol{x}_n \times \boldsymbol{v}_n, \quad (5)$$

where $\boldsymbol{x}_n$ and $\boldsymbol{v}_n$ are the position and velocity vectors of particle n relative to the halo centre and the centre-of-mass velocity. We compute $\boldsymbol{j}_{\rm gal}$ for $r \leq 0.1 r_{200}$ (using only the star particles) to characterize the inner galaxy. The stress or velocity dispersion tensor of the dark matter distribution is

$$\Pi_{ij} = \sum_{n=1}^{N \leq r} v_{i,n} v_{j,n}. \quad (6)$$

We can diagonalize this tensor to find the eigenvectors and eigenvalues which define the principal velocity anisotropy axes ($a_{\rm vel}$, $b_{\rm vel}$, $c_{\rm vel}$).

In Fig. 2, we show the median misalignment angles between the galaxy and the dark matter halo as a function of radius. The top left-hand panel shows the misalignment in angular momentum, the top right-hand panel the misalignment in shape. Note that the angular momentum or shape of the galaxy is always calculated for $r \leq 0.1 r_{200}$, whereas the computation of the dark matter halo properties varies with radius. There is strong alignment of angular momentum vectors in the inner regions of the halo, but the median misalignment gradually increases to $\approx 40^\circ$ at $r \sim r_{200}$. This is in good agreement with Bett et al. (2010) who find a median misalignment of $\sim 30^\circ$ for a smaller sample of $\sim$50 haloes. There is also strong alignment between the short axis of the galaxy and the short axis of the dark matter halo where the median misalignment grows to $\approx 20^\circ$ at $r \sim r_{200}$. In the bottom left-hand panel, we see that the alignment between the major axes of the galaxy and dark matter halo is poorer and there is significant scatter. This is not surprising as for disc-like configurations the major axis is poorly defined (i.e. $q = b/a \approx 1$). The bottom right-hand panel shows the alignment between the short axis and the angular momentum vector of the dark matter halo as a function of radius (shaded green). We also show as the shaded red region the alignment between the short axis of the dark matter halo shape and the short axis of the velocity dispersion tensor. There is a very strong alignment between the shape and velocity dispersion. This reflects the fact that the dark matter halo shape is supported by internal velocities rather than net rotation (Frenk et al. 1988).

To avoid any ambiguity in the definition of the short axes or angular momentum vectors of the dark matter haloes, Bett et al. (2010) imposed constraints on their shapes and net angular momentum ($s < 0.81$, $\log_{10} j(\leq r_{200})/\sqrt{G M_{200} r_{200}} \geq -1.44$). With these restrictions, we see stronger alignments in general between the galaxy and dark matter halo. This is not surprising, as we have found that the dark matter haloes are close to spherical and are mainly dispersion, rather than rotationally, supported. However, we choose to include all of our haloes to avoid selection biases (only $\sim$40 per cent of our sample satisfy the constraints), but check that our main results are not significantly altered by discarding dark matter haloes that have little net rotation and are close to spherical.

Further insight into the misalignment between the galaxy and dark matter halo can be gained by examining the distribution of these misalignment angles at different radii. In Fig. 3, we show the distributions of misalignments between the galaxy and dark matter halo angular momentum vectors (top panels) and short axes (bottom panels) both for $r \leq 0.1 r_{200}$ (left-hand panels) and for $r \leq r_{200}$ (right-hand panels). As we already saw in Fig. 2, there is much stronger alignment in the inner regions of the halo. However, when the shape of the dark matter halo is computed for $r \leq r_{200}$, the short axis of the inner galaxy is misaligned from the short axis of the dark matter halo by $\theta > 45^\circ$ in approximately 30 per cent of the systems. The orientation of the angular momentum vector of the galaxy is aligned almost perpendicularly ($45^\circ < \theta < 135^\circ$) to the net spin of the dark matter halo in approximately 40 per cent of the systems and 2 per

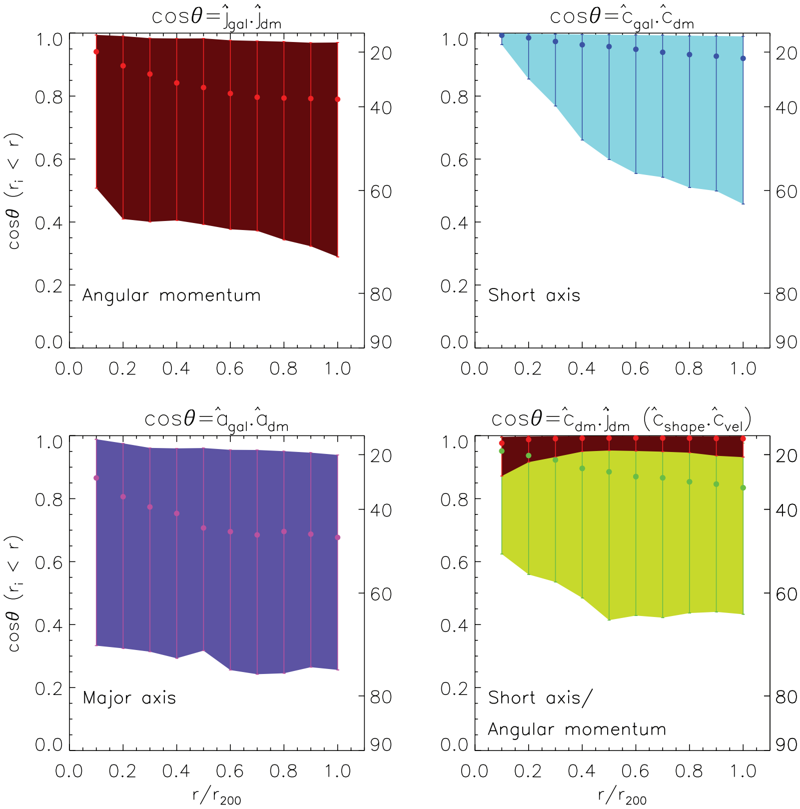

Figure 2. Median misalignment angles as a function of radius. Error bars and shaded regions show the values covered by 68 per cent of the distribution (i.e. the 1σ dispersion). Top left-hand panel: misalignment angles between the angular momentum vector of the galaxy ($\hat{j}_{\rm gal}$) and the angular momentum vector of the dark matter halo ($\hat{j}_{\rm dm}$). Top right-hand panel: misalignment angle between the short axis of the galaxy ($\hat{c}_{\rm gal}$) and the short axis of the dark matter distribution ($\hat{c}_{\rm dm}$). Bottom left-hand panel: misalignment angles between the major axis of the galaxy ($\hat{a}_{\rm gal}$) and the major axis of the dark matter distribution ($\hat{a}_{\rm dm}$). Bottom right-hand panel: misalignment angles between the short axis and the angular momentum vector of the dark matter distribution (green shaded region). For comparison, the misalignment between the short axis of the velocity anisotropy tensor ($\hat{c}_{\rm vel}$) and the short axis of the dark matter halo shape ($\hat{c}_{\rm shape}$) is shown by the red shaded region. There are strong alignments between the galaxy and the dark matter halo at small radii ($r \sim 0.1r_{200}$) but there can be significant misalignments at larger radii ($r \sim r_{200}$).

cent are even anti-aligned. Our results are in good agreement with Bailin et al. (2005) who analyse the shape and internal alignment of the dark matter haloes of seven high-resolution cosmological disc galaxy formation simulations. The authors find that while the minor axis of the inner dark matter halo ($r \leq 0.1r_{200}$) is well aligned with the disc axis, the outer regions of the halo can be substantially misaligned.

The misalignments between the galaxy and the dark matter halo have potential implications for galaxy–galaxy weak lensing studies. Such studies attempt to deduce the weak cosmological signal from the observed galaxy ellipticity correlation. Typically the influence of any intrinsic signal on the observed ellipticity correlation is neglected. However, correlations between halo shape and the density field are expected to arise through tidal torques operating during galaxy formation (e.g. Heavens & Peacock 1988). More recent work has attempted to quantify the potential sources of lensing contamination caused by these intrinsic alignments by examining dark matter only cosmological simulations (e.g. Heymans et al. 2006). Any misalignments between the galaxy and the dark matter halo will weaken the expected intrinsic signal deduced from dark matter only simulations.

What causes these misalignments between the galaxy and the outer dark matter halo? According to tidal torque theory (e.g. Fall & Efstathiou 1980; White 1984), the angular momentum of the galaxy and the dark matter halo is initially very well aligned. However, the outer halo continues to accrete material, which can alter its shape and/or its net angular momentum. Hence, whilst we see strong alignment in the inner regions of the halo, there can be significant misalignments in the outer parts. This has important implications for the satellite populations of these haloes. The majority of the satellite galaxies are located in the outer regions of the halo. It is to this topic that we now turn.

4 SATELLITE GALAXIES

Here, we study the spatial and velocity distributions of the satellite systems of our simulated galaxies, focusing on their alignment (in positional and velocity space) with the parent dark matter halo and galaxy.

In Fig. 4, we show the cumulative number distribution of satellite galaxies (red) and dark matter (blue) within r_{200}. We have stacked all of the satellite galaxies by normalizing their radial distances from the parent halo centre by r_{200}. The density profiles for both the dark matter particles and satellite galaxies can be described (Navarro et al. 2004) by

$$\ln\rho(r) \propto -(2/\alpha)[(r/r_c)^{\alpha} - 1]. \quad (7)$$

This density profile was first introduced by Einasto (see e.g. Einasto & Haud 1989) and is mathematically equivalent to the Sersic profile that is often used to describe the projected density profile of galaxies.

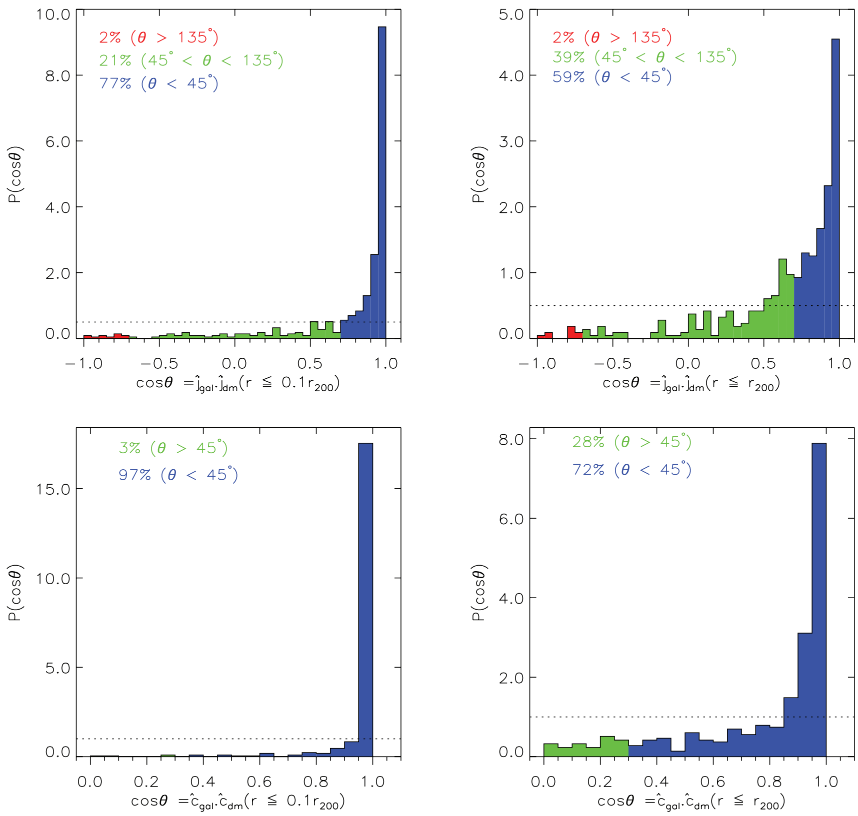

Figure 3. Top: the distribution of misalignment angles between the angular momentum of the galaxy and the angular momentum of the dark matter halo for $r \le 0.1r_{200}$ (left-hand panel) and $r \le r_{200}$ (right-hand panel), respectively. Bottom: the distribution of misalignment angles between the short axis of the galaxy and the short axis of the dark matter halo for $r \le 0.1r_{200}$ (left-hand panel) and $r \le r_{200}$ (right-hand panel), respectively. The dotted lines show a uniform distribution.

Low values of the power-law slope (α) describe a 'cuspy' density profile. In agreement with previous work (e.g. Navarro et al. 2004; Gao et al. 2008), we find a dark matter density slope of $\alpha_{\rm dm} \sim 0.2$. In contrast, the satellite distribution favours larger values of α and has a 'cored' profile. As found many times before (e.g. Libeskind et al. 2005; Zentner et al. 2005; Ludlow et al. 2009), there is an obvious spatial bias between the dark matter and the satellite galaxy population.

Fig. 4 also shows the cumulative number of satellites with stellar mass fractions greater than 2 per cent and less than 2 per cent by the magenta and cyan dotted lines, respectively.[1] Satellites with higher stellar mass fractions are more centrally located. These are generally the most massive satellites which have spiralled into the central regions of the halo during the course of several pericentric passages. The stellar component of satellite galaxies is more centrally located than the dark matter distribution. Whilst the dark matter 'envelope' is more effectively tidally stripped, the stellar component remains relatively undisturbed. Libeskind et al. (2010) showed that the increased density in the central regions of a subhalo due to the collapse of baryons leads to a reduced mass loss relative to an equivalent dark matter only satellite (see also Macciò et al. 2006). Dynamical friction is thus more effective and satellites sink closer into the parent halo. This leads to a more centrally concentrated distribution of satellite galaxies when baryons are included. By comparison with our dark matter only simulations, we also see a more substantial inner radial bias when baryons are included (see bottom panel of Fig. 4). Note that this effect is not as pronounced for the lower mass satellites, which are less affected by dynamical friction.

The bottom panel of Fig. 4 shows the cumulative number distribution of the 10 brightest (i.e. highest stellar mass) satellites within r_{200} for individual systems. Approximately 80 haloes have at least 10 satellites within r_{200}. We limit ourselves to the 10 brightest satellites to enable comparison with the data on the Milky Way and M31. The positional data for the Milky Way and M31 satellites are taken from tables 3 and 5 of Deason, Belokurov & Evans (2011) (see references therein). Although the top panel of Fig. 4 gives no indication of the scatter in the simulations, the bottom panel explicitly shows the system-to-system variation (encompassed by the blue hatched region). The solid red and green lines give the profiles for the classical Milky Way satellites and the 10 brightest M31 satellites (within r_{200}). We use the r_{200} values for the Milky Way and M31 recently estimated by Guo et al. (2010) of approximately 250 and 290 kpc, respectively.[2] The profiles for both M31 and the Milky Way lie within the scatter of the simulations. In particular, there is very good agreement with M31 for which (owing to our external view) there are less biases in the observed sample. Note that Font et al. (2011) show in their fig. 1 that the luminosity function of the satellite galaxies in GIMIC is also in good agreement with the satellite systems of Local Group galaxies.

[1] We verified that our results are not substantially affected if we choose fractional stellar mass limits of 1.5 or 2.5 per cent

[2] These were computed using the estimated halo masses given in table 1 of Guo et al. (2010) and then their equation (1) was used to estimate r_{200}.

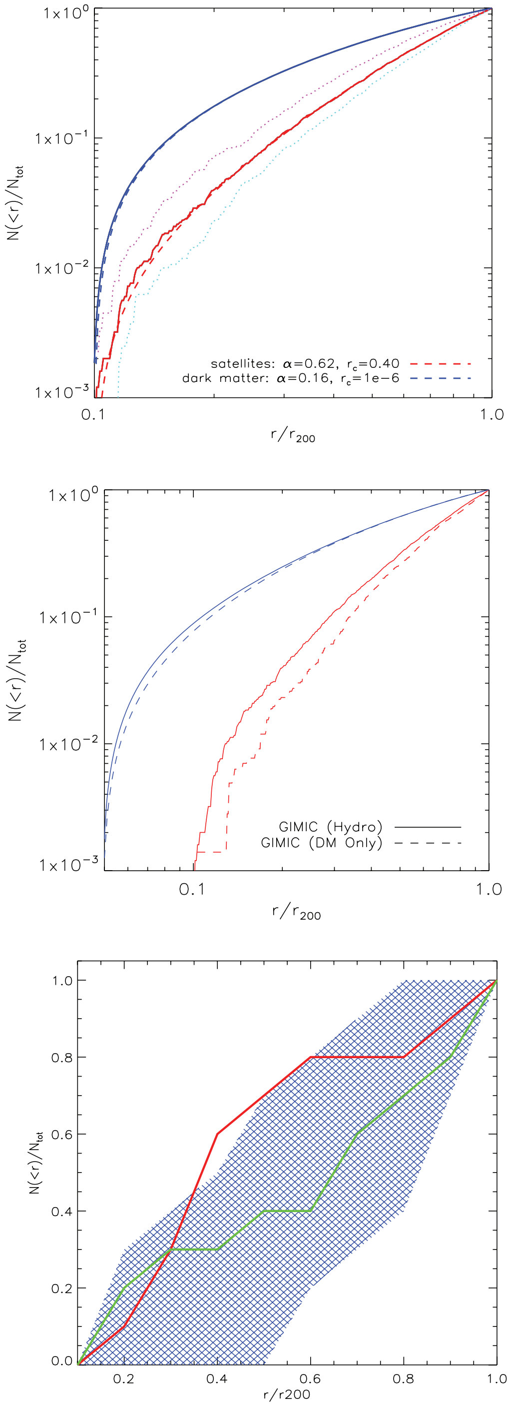

Figure 4. Top panel: the cumulative number distribution for satellites (full red line) and dark matter particles (full blue line) within r_{200}. Fits to Einasto profiles are given by the red and blue dashed lines. The dotted magenta and cyan lines show the cumulative number distribution for satellites with stellar mass fractions, $M^*_{\rm sat}/M_{\rm sat}$, greater than 2 per cent and less than 2 per cent, respectively. Middle panel: the red and blue lines give the radial profiles of the satellites and dark matter particles, respectively. The dashed lines show the profiles for the dark matter only counterparts of our sample of haloes. Bottom panel: the cumulative number distribution for the 10 brightest satellites of individual systems. The blue hashed region encompasses the scatter of the profiles for the ∼80 systems with 10 or more satellites within r_{200}. The red and green lines give the profiles for the classical Milky Way satellites and the 10 brightest M31 satellites (within r_{200}), respectively.

4.1 Anisotropic distributions

Here, we first restrict attention to host galaxies which have 10 or more associated satellites within r_{200} (cf. Libeskind et al. 2007, 2009). For comparison with the classical satellites of the Milky Way (and M31), we consider the 10 brightest (i.e. highest stellar mass) satellites in each system. We compute the shape ($a_{\rm sat}$, $b_{\rm sat}$, $c_{\rm sat}$) of the satellite galaxy distribution within r_{200} of each host galaxy by diagonalizing the second moment tensor defined as

$$I^*_{ij} = \sum_{n=1}^{N(\leq r)} x_{i,n} x_{j,n}. \qquad (8)$$

This is used in preference to the reduced inertia of equation (1) which requires an iterative algorithm to discard outliers until convergence is achieved. For systems of satellites with a small number of data points, this is undesirable.

In the left-hand panel of Fig. 5, we show that the satellite distribution is generally more flattened than the underlying dark matter distribution. The red dot indicates the median axial ratio values for the satellites and dark matter ($\langle s_{\rm sat}\rangle \sim 0.5$, $\langle s_{\rm dm}\rangle \sim 0.8$). We show with the blue arrow the range of values for the flattening of the Milky Way dark halo given in the literature. We suggest the difference in flattening may be understood by considering when the dark matter was accreted relative to the satellite galaxies. Present-day satellites are the surviving population, and have had been in orbit for much less time than the dark matter (see Section 4.4). As far as the satellites are concerned, the potential of the halo has largely been static since accretion. The dark matter, by contrast, has undergone relaxation and phase mixing. Even though both the satellites and dark matter are accreted anisotropically, this will be reflected to a greater degree in the spatial distribution of the satellite galaxies rather than the dark matter halo. The right-hand panel of Fig. 5 shows the distribution of axial ratios for the satellite systems. The blue and green stars show the flattening for both the classical Milky Way satellites and the 10 brightest M31 satellites computed in the same way as the simulated satellites. The classical Milky Way satellites have a highly flattened distribution which is consistent (within 2σ) with the median value derived from the simulations, whilst the M31 satellites have a less flattened configuration and lie closer to the median $s = c/a$ value. The points are coloured according to the alignment of the satellite distribution with the galaxy (see below and Fig. 6). Polar ($\hat{c}_{\rm gal}.\hat{c}_{\rm sat} < 0.25$), planar ($\hat{c}_{\rm gal}.\hat{c}_{\rm sat} > 0.75$) and 'in-between' ($0.25 < \hat{c}_{\rm gal}.\hat{c}_{\rm sat} < 0.75$) alignments are given by the magenta, cyan and black points, respectively. There is no obvious correlation between the orientation of the satellite distribution and their flattening. Neither does there seem to be a bias towards a particular orientation, as we discuss below.

We show the distribution of alignments between the short axes of the satellite systems and the short axes of the dark matter halo (for $r \leq r_{200}$) and the galaxy of their parent haloes in Fig. 6. The orientation of each satellite system with respect to its host dark matter distribution and galaxy is shown in the right-hand and left-hand panels, respectively. The satellite distribution preferentially aligns in a plane perpendicular to the short axis of the dark matter distribution. However, the satellites show no preferential alignment relative to the galaxy. There are a significant number of systems where the satellite distribution is aligned in a plane perpendicular to the disc (20 per cent of the systems have $\cos\theta < 0.2$ or $\theta > 80°$). Thus, the alignment of the Milky Way satellites perpendicular to the disc plane is not inconsistent with the results we present here. The red dashed lines give the distributions when

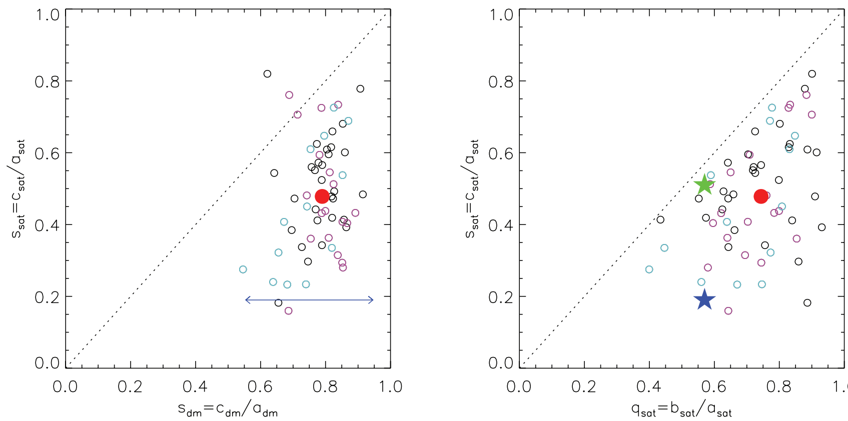

Figure 5. Left-hand panel: the shape of the satellite distribution and underlying dark matter haloes as defined by the sphericity, $s = c/a$. Only haloes with 10 or more satellites within r_{200} are considered and the shape is computed for the 10 highest stellar mass satellites. The red dot indicates the median values, whilst the blue line indicates the approximate values for the Milky Way (the blue arrows denote the uncertainty in the sphericity of the dark matter halo of the Milky Way). The points are colour coded according to the alignment between the system of satellites and the galaxy. Cyan, magenta and black points are for satellite systems where $\hat{c}_{\rm gal}.\hat{c}_{\rm sat} > 0.75$, $\hat{c}_{\rm gal}.\hat{c}_{\rm sat} < 0.25$ and $0.25 < \hat{c}_{\rm gal}.\hat{c}_{\rm sat} < 0.75$, respectively. The satellite galaxies generally have a more flattened spatial distribution than the dark matter. Right-hand panel: the axial ratios of the satellite distribution. The blue and green stars indicate the axial ratios for the classical Milky Way satellites and the 10 brightest M31 satellites (within r_{200}).

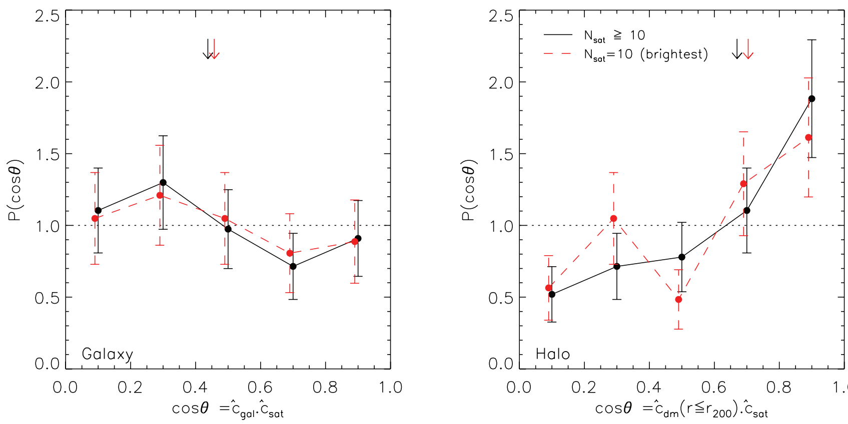

Figure 6. The orientation of the short axes of the satellite distribution relative to the short axes of the parent galaxy and dark matter halo (defined within r_{200}). The black lines are for all systems of satellites with 10 or more satellites within r_{200}. The red dashed lines give the distributions when only the 10 brightest satellites within r_{200} are used to compute the shapes of the satellite distribution. Downward pointing arrows denote the median of the distributions and the dotted lines indicate a uniform distribution. The error bars denote Poisson uncertainties. Whilst there is strong alignment between the spatial distribution of the satellite galaxies and the dark matter halo, the distribution with respect to the galaxy is consistent with isotropy.

only the 10 brightest satellites within r_{200} are used to compute the shapes of the satellite distribution. Although there is substantial uncertainty caused by small number statistics, we can see that by restricting ourselves to the same number of satellites as the observational sample (and naively ignoring selection biases), the apparent distribution of Milky Way satellites is consistent with the simulations.

In Table 2, we give the number of satellite systems which have similar (perpendicular) orientations as the Milky Way Galaxy. Our results are robust to more restrictive *D*/*T* cuts. In fact, the fraction of systems with almost perpendicular satellite alignments is slightly higher for parent galaxies with $D/T > 0.7$. Our total mass range ($5 \times 10^{11} < M_{200}/\mathrm{M}_{\odot} < 5 \times 10^{12}$) is broadly coincident with the masses of the Milky Way and M31. We can further refine our sample selection by using haloes with stellar masses similar to these local galaxies. In the bottom row of Table 2, we give the number of satellite systems with polar alignments which also have parent stellar masses within a factor of 2 of the observed estimates for the Milky Way and M31 ($2.5 \times 10^{10} < M^{*}/\mathrm{M}_{\odot} < 2 \times 10^{11}$; e.g.

Table 2. The number of parent haloes in the mass range $5 \times 10^{11} < M_{200} < 5 \times 10^{12}$ for different *D*/*T* cuts. We give the total number of parent haloes, the number of haloes with at least 10 satellites within r_{200}, the number of satellite systems inclined by more than 80° to the galaxy and the number of these systems which have similar stellar masses $M^{\star}$ (within a factor of 2) to the Milky Way and M31 ($\sim M_{\rm MW}$). Our results are robust to more restrictive *D*/*T* cuts. Approximately 20 per cent of satellite systems (with at least 10 members) are aligned perpendicularly to their parent galaxy.

D/*T*	>0.3	>0.5	>0.7
$N_{\rm tot}$	431	328	192
$N(N_{\rm sat} \geq 10)$	86	68	51
$N(N_{\rm sat} \geq 10, \theta > 80^{\circ})$	20	16	15
$N(N_{\rm sat} \geq 10, \theta > 80^{\circ}, M^{\star} \sim M_{\rm MW})$	15	13	12

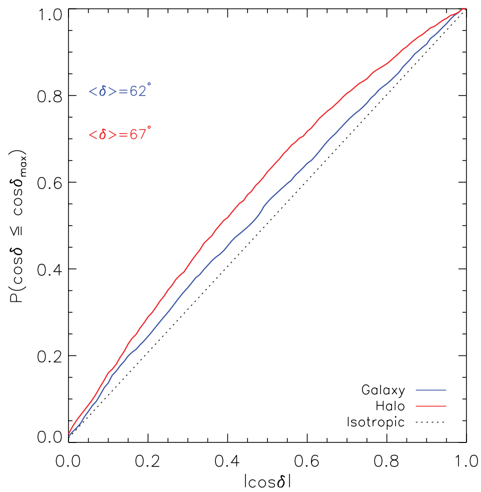

Figure 7. The cumulative probability distribution for the location of satellites relative to the host minor axis. Here, we consider *all* satellites within r_{200} and are not restricted to those systems with large numbers of satellites. δ is defined from the minor axis (i.e. $\delta = 0$ is polar alignment, $\delta = 90°$ is planar alignment). The blue distribution is relative to the short axis of the galaxy (or disc) and the red distribution is relative to the short axis of the dark matter halo (defined for $r \le r_{200}$). There is a preference for planar alignment relative to the dark matter halo but there is a much weaker correlation with the galaxy.

Widrow, Perrett & Suyu 2003; Geehan et al. 2006; Hammer et al. 2007). Independently of our *D*/*T* cut, we find that approximately 20 per cent of disc galaxies with similar masses as the Milky Way and M31 have satellite systems with polar alignments relative to the galaxy.

In Fig. 7, we show the probability distribution of the orientation of the satellite galaxies relative to their host. This differs from the previous calculation, as we consider all of the satellite galaxies and stack them together (cf. Brainerd 2005; Yang et al. 2006). We show the cumulative probability distribution of δ, which is defined as the angle between the short axis of the host and the position vector of a satellite galaxy (i.e. $\delta = 0$ is polar alignment and $\delta = 90°$ is planar alignment). The blue and red lines are relative to the minor axis of the galaxy and the minor axis of the dark matter halo, respectively. An isotropic distribution is shown by the dotted line. The satellites exhibit a roughly planar alignment relative to the dark matter distribution, in agreement with the right-hand panel of Fig. 6 where we consider only systems with a large number of satellites. The satellites have a relatively weaker alignment relative to the inner disc, although there is a slight bias towards planar alignment. It is interesting that we find qualitatively similar results to Brainerd (2005) and Yang et al. (2006) who, owing to the small number of satellite galaxies per parent halo, use stacked samples of satellites to generate a probability distribution of their orientations with respect to their hosts. However, a direct comparison is difficult due to the different halo selection criteria used by these authors.

4.2 Rotational support

It has been suggested that the satellites of the Milky Way lie in a rotationally supported disc (e.g. Kroupa et al. 2005; Metz et al. 2008). We calculate the rotational velocity in the plane perpendicular to the short axis of the satellite distribution ($c_{\rm sat}$), $\langle v_{\phi'} \rangle$, and find the velocity dispersion in this plane ($\sigma_{\phi'}$). Typical values of these quantities are $\langle v_{\phi'} \rangle = 40\,{\rm km\,s^{-1}}$ and $\sigma_{\phi'} = 150\,{\rm km\,s^{-1}}$. The left-hand panel of Fig. 8 shows a histogram of the ratio of this net rotational velocity to the velocity dispersion. Note that here we are restricted to satellite systems with 10 or more members and focus on the 10 brightest satellites within r_{200}. The majority of satellite systems are not rotationally supported and their kinetic energy is dominated by internal motions. However, there are a small fraction (∼9 per cent) of systems that show substantial rotational support with $|\langle V_{\phi'} \rangle|/\sigma_{\phi'} > 0.8$.

Further investigation into these rotationally supported systems of satellites suggests that a significant fraction of the satellites are accreted in groups (i.e. from similar directions at the same time). We give an example in the middle panel of Fig. 8. This system of satellites defines a highly flattened plane at $z = 0$ ($s_{\rm sat} \sim 0.25$) and shows evidence of substantial rotational support with $|\langle V_{\phi'} \rangle|/\sigma_{\phi'} \sim 0.9$. The radial trajectories of some of the satellites belonging to this system are shown in Fig. 8. We can see that four of the satellites infall as a group at $z \sim 0.6$ (or $t_{\rm lookback} \sim 6$ Gyr). The coherency of the angular momenta of this group of satellites is retained until $z = 0$ (cf. Li & Helmi 2008). Hence, signatures of rotational support are closely linked to systems of satellites where a substantial number of the satellite population today were accreted as a group. Metz et al. (2009) argue that the majority of the Milky Way satellites did not enter the halo in a group based on comparisons with dwarf associations in the Local Group (found by Tully et al. 2006). Our result suggests a link between group infall and rotational support but does not directly address the issue of group infall into the Milky Way itself.

Metz et al. (2008) remark that at least three of the classical Milky Way satellites have orbital poles which lie within 30° of the short axis of the so-called disc of satellites. In the right-hand panel of Fig. 8, we show the distribution of the number of satellites with orbital poles within 15°, 30° and 45° (red, black and blue lines) of the short axis of their spatial distribution. In ≈20 per cent of the systems, three satellites have orbital poles within 30° of the normal to their spatially defined distribution. However, no systems have more than seven (out of 10) satellites which all have orbital poles within 30°. Thus, in agreement with Libeskind et al. (2009), we find that an arrangement whereby the majority of the classical Milky Way satellites have orbital poles well aligned with the short axis of their flattened distribution will be difficult to reconcile with the results presented here. For comparison, we show with the dashed black line the case for an isotropic distribution of satellites in both positional and velocity space. The fraction of systems with more than two satellites with orbital poles within 30° of the short axis of their spatial distribution is reduced in the isotropic case. This reinforces the point that the satellites are not randomly distributed in phase space.

4.3 Angular momentum orientation

The specific angular momenta of the satellites are computed using equation (5). In this case, we consider our whole sample of satellite galaxies and are not restricted to parent haloes with a large number of satellite galaxies.

The top panels of Fig. 9 show the distribution of the angles between the angular momentum vector of each individual satellite and the angular momentum of the dark matter halo [$\hat{j}_{\rm dm}(r \le r_{200})$, left-hand panel] and the angular momentum of the galaxy [$\hat{j}_{\rm gal}(r \le 0.1 r_{200})$, right-hand panel]. There is an obvious bias in both cases towards alignment between the angular momentum

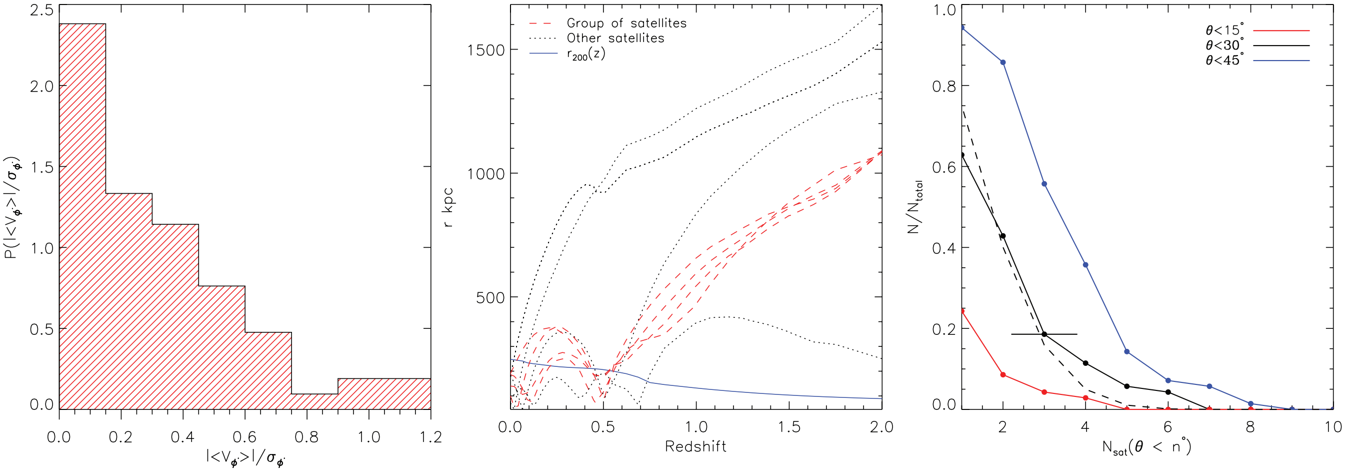

Figure 8. Left-hand panel: the probability distribution, $P(|\langle V_{\phi'}\rangle|/\sigma_{\phi'})$, for the ratio of rotational versus dispersion support for each system of satellites where $N_{\rm sat}(r \le r_{200}) > 10$. We only consider the 10 brightest satellite galaxies within r_{200}. The median rotation velocity ($\langle V_{\phi'}\rangle$) and dispersion ($\sigma_{\phi'}$) are calculated in the plane perpendicular to the short axis of the satellite distribution. Middle panel: the radial trajectory of a system of satellites exhibiting rotational support at $z = 0$. A group of satellites is accreted at $z \sim 0.6$ (red dashed lines). This group dominates the signature of rotational support shown at $z = 0$. Dotted lines show the trajectories of some of the other satellites and the solid blue line indicates $r_{200}(z)$. Right-hand panel: the fraction of systems ($N/N_{\rm total}$) where the orbital poles of $N_{\rm sat}$ satellites lie within 15° (red line), 30° (black line) and 45° (blue line) of the short axis defined by the spatial distribution of satellites. The horizontal black line indicates the fraction of systems which have three satellites with orbital poles within $\theta < 30°$. The dashed black line shows the case for $\theta < 30°$ for an isotropic distribution of satellites (in both positional and velocity space).

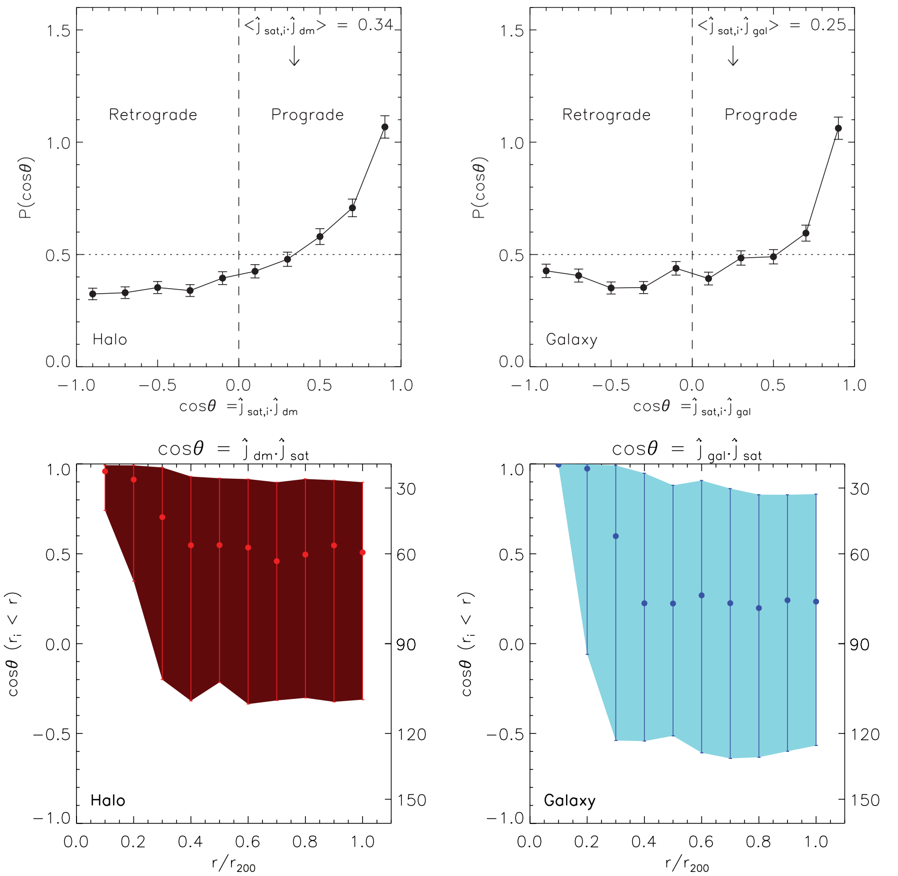

Figure 9. Top panels: alignment between the angular momentum vector of each individual satellite galaxy ($\hat{j}_{\rm sat,i}$) and its parent dark matter halo [$\hat{j}_{\rm dm}(r \le r_{200})$, left-hand panel] and galaxy [$\hat{j}_{\rm gal}(r \le 0.1r_{200})$ right-hand panel]. Downward pointing arrows give the median values and the error bars denote Poisson uncertainties. Bottom panels: the median alignment values between the angular momentum vectors of the satellite galaxies and their parent dark matter halo (left-hand panel) and galaxy (right-hand panel) as a function of radius. Error bars and shaded regions encompass the values covered by 68 per cent of the distribution. There is a bias towards co-rotation (relative to both the spin axis of the dark matter halo and the spin axis of the disc) which is more pronounced in the inner regions of the halo.

vectors. With respect to the angular momentum of the disc (dark matter), approximately 61 per cent (68 per cent) of the satellites are on 'prograde' orbits ($\cos\theta > 0$) and 39 per cent (32 per cent) are on 'retrograde' orbits ($\cos\theta < 0$). This is in agreement with recent work by Lovell et al. (2011) who analysed the orbital angular momentum of dark matter subhaloes in the Aquarius simulations. All six of the parent haloes in this study contain populations of co-rotating subhalo orbits. In addition, three of their parent haloes contain subhaloes on retrograde orbits. The authors attribute these configurations to the filamentary accretion of subhaloes.

Whilst we see a bias towards co-rotating orbits relative to the inner galaxy, the spatial orientation of the satellites is only weakly related to the orientation of the disc. For most satellite systems, there is little correlation between their shape and net angular momentum (only a small fraction are rotationally supported). In addition, phase-space mixing is more rapid in spatial coordinates than velocity space – the angular momentum orientation of the satellites will be preserved for longer than any spatial anisotropy. This is especially true for satellites accreted at earlier times.

In the bottom panels of Fig. 9, we show the radial dependence of the alignment between the satellite angular momenta and the dark matter halo angular momenta (left-hand panel) and the galaxy angular momenta (right-hand panel). The angular momenta of the satellite galaxies are more closely aligned with the dark matter than the inner galaxy. The continual accretion of material can alter the orientation of the net spin of the halo at larger radii. The accretion of satellites is closely linked to the spinning up of the dark matter halo (e.g. Vitvitska et al. 2002); hence, it is unsurprising that the satellite angular momenta are well aligned with the dark matter spin. We found in Section 3.2 that there can be substantial misalignments between the angular momentum of the galaxy and the net spin of the outer dark matter halo. Hence, the angular momenta of the satellite galaxies are less strongly related to the galaxy (this is especially true for those satellites accreted at later times).

We find that there is a more pronounced bias towards satellites on co-rotating orbits (relative to both the disc and dark matter halo) in the inner regions of the halo. We relate this radial dependence to the accretion history of the satellite galaxies in the following section. Note that Hwang & Park (2010) use a sample of SDSS galaxies to study the rotation of satellite galaxies relative to the spin of their host galaxy. The authors also find a stronger bias towards co-rotating orbits in the inner regions of their host galaxies.

4.4 Anisotropic accretion

The redshift $z = 0$ population of satellites is preferentially aligned in the plane perpendicular to the short axis of the dark matter distribution and exhibits a bias towards co-rotating orbits (with respect to both the net spin of the dark matter and the inner galaxy). Both these observations hint that the satellite galaxies are accreted from preferential directions (e.g. filaments, Libeskind et al. 2005). According to tidal torque theory, the angular momentum of a halo is acquired through the tidal interactions between neighbouring structures (out to 20 Mpc) and infalling subhaloes. Presumably some of the surviving population of satellites today were accreted in a similar fashion and from similar directions as those subhaloes which originally spun up the halo. Thus, the bias towards co-rotating orbits can be explained by tidal torque theory whereby the satellite population today bears the imprint of those subhaloes which were accreted from similar directions as the substructures involved in the early stages of galaxy formation.

We trace back our $z = 0$ population of satellite galaxies to $z = 2$.[3] Our results are summarized in Fig. 10. Note that we align our coordinate system with respect to the galaxy at $z = 0$ and $\hat{j}_{\rm gal}$ is defined at $z = 0$. The top left-hand and middle panels show the percentage of prograde (red) and retrograde (blue) satellite orbits as a function of the radial distance from the parent galaxy at $z = 0$ and as a function of the time at which the satellite was accreted. We define the 'accretion' time when a satellite first crosses over $r_{200}(z)$. Similarly, the bottom left-hand and middle panels show the median misalignment between the galaxy angular momentum (defined at $z = 0$) and the satellites' angular momenta as a function of radial distance and accretion time. We see a stronger bias towards prograde orbits for those satellites accreted at larger lookback times. In addition, those satellites located closer into the parent halo have a stronger tendency to be prograde that those located further out. The top right-hand panel shows the median satellite $V_{\rm max}$, the peak of the satellite's circular velocity profile, at the time of accretion as a function of the radial distance from the parent galaxy today. Satellites located closer into the parent halo are on average more massive at the time of accretion. The bottom right-hand panel shows the median alignment angle between the satellite angular momenta and the galaxy as a function of the satellite's $V_{\rm max}$ at the time of accretion. The most massive satellites at accretion tend to have a stronger alignment with the net angular momentum of the galaxy.

These results support the suggestion that the bias towards co-rotating orbits is a consequence of the hierarchical assembly of galaxies. We find that more massive satellites accreted at earlier times are more strongly biased towards co-rotation. These satellites resemble the early substructures which originally spun up the halo. The stronger bias towards co-rotating satellites in the inner regions of the halo can be explained by the prevalence of the most massive satellites *at accretion* in these regions at $z = 0$. By dynamical friction effects, we expect the more massive satellites to sink into the centre of the parent halo on shorter time-scales than those with lower masses.

In Fig. 11, we show the 2D projection of the infall direction of the satellite population at $z = 0$. In the left-hand panel, θ and ϕ are the polar and equatorial axes defined with respect to the plane of the disc.[4] In the right-hand panel, θ and ϕ are defined relative to the dark matter shape (the shape is computed for $r \leq r_{200}$). We define a spherical surface at $r = r_{200}(z)$ and calculate θ and ϕ when a satellite crosses this surface. We stack all the haloes in our sample where $\theta = 0$ defines either the plane of the disc (left-hand panel) or the plane perpendicular to the short axis of the dark matter halo (right-hand panel). There is a preference for accretion in a plane perpendicular to the short axis of the dark matter distribution. The bottom inset panel shows the fractional number of satellites accreted as a function of ϕ – this shows there is a preference for accretion along the major axis of the dark matter halo (i.e. $|\phi| = 0$, $180°$ or $\pm x$). This is in agreement with Libeskind et al. (2005) and Zentner et al. (2005) who find a preferential direction of satellite accretion along the major axis of the halo and Bailin & Steinmetz (2005b) who find that there is a strong tendency for the minor axes of haloes to lie perpendicular to large-scale filaments. There is a much weaker bias relative to the disc plane. In Section 4.1, we

[3] We do not trace our sample of satellites beyond redshift $z = 2$ as only a very small fraction of satellites accreted before this epoch have survived until $z = 0$.

[4] The angle ϕ is defined relative to the major axis of the galaxy but note that as $b/a \sim 1$ for a disc this is a rather ambiguous definition.

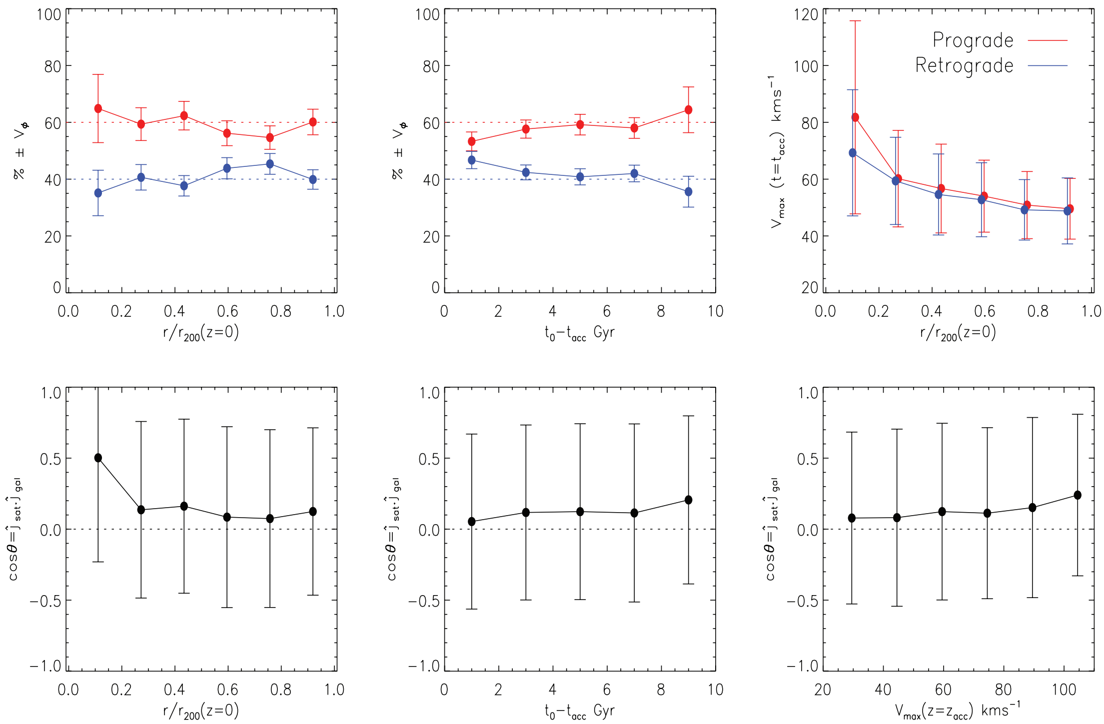

Figure 10. Top left-hand panel: the percentage of satellites on prograde (red) and retrograde (blue) orbits as a function of radial distance from the parent halo at $z = 0$. The dashed horizontal lines denote a ratio of 60:40. Error bars give Poisson uncertainties. Bottom left-hand panel: the median alignment between the satellite angular momenta and the galaxy as a function of radial distance at $z = 0$. The error bars indicate the dispersion in the distributions. Top middle panel: the percentage of satellites on prograde (red) and retrograde (blue) orbits as a function of accretion time. Bottom middle panel: the median alignment between the satellite angular momenta and the galaxy as a function of when they were accreted. Top right-hand panel: the median satellite $V_{\rm max}$ at the time of accretion as a function of radial distance from the host at $z = 0$. Bottom right-hand panel: the median alignment between the satellite angular momenta and the galaxy as a function of satellite $V_{\rm max}$ at the time of accretion. A stronger bias towards prograde orbits is seen by satellites accreted at early times and by those satellites which were relatively massive at the time of accretion.

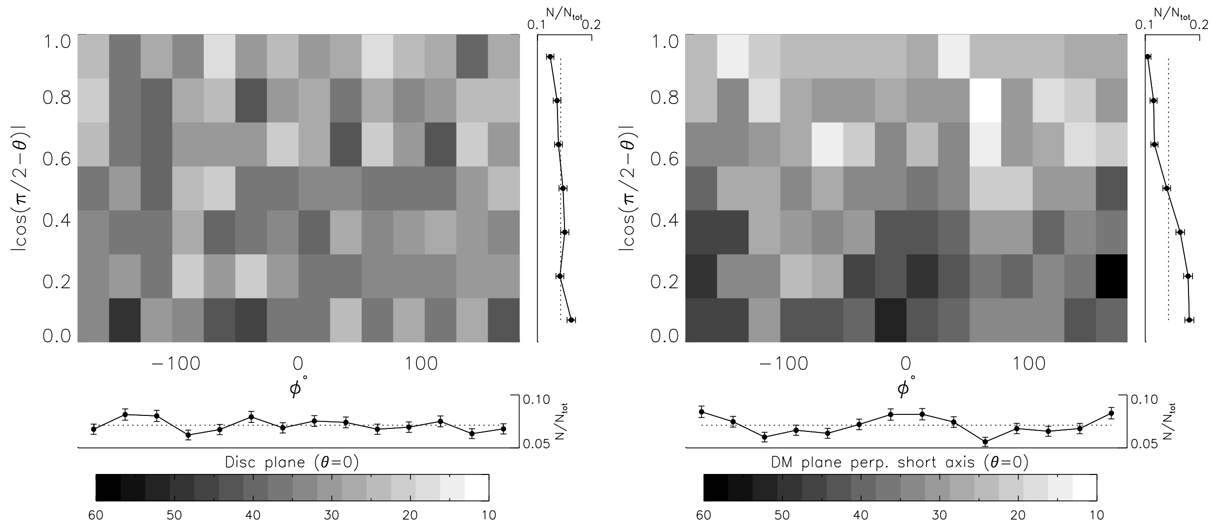

Figure 11. The projection in $\cos(\pi/2 - \theta)$ and ϕ of the direction of satellite accretion. θ and ϕ are the polar and equatorial axes as defined in the disc plane (left-hand panel) at $z = 0$ or defined relative to the dark matter halo shape (right-hand panel) at $z = 0$. The right and bottom inset panels give the fractional number of satellites accreted as a function of θ and as a function of ϕ, respectively. Note that the dark matter halo shape is defined for $r \le r_{200}$. The positions on the sky are calculated when a satellite passes inside $r_{200}(z)$ for the first time. The scale bar gives the number of satellites in each pixel. There is a preference for satellite accretion in a plane perpendicular to the short axis of the dark matter halo (as defined at $z = 0$ for $r \le r_{200}$) but there is a very weak correlation with the galaxy.

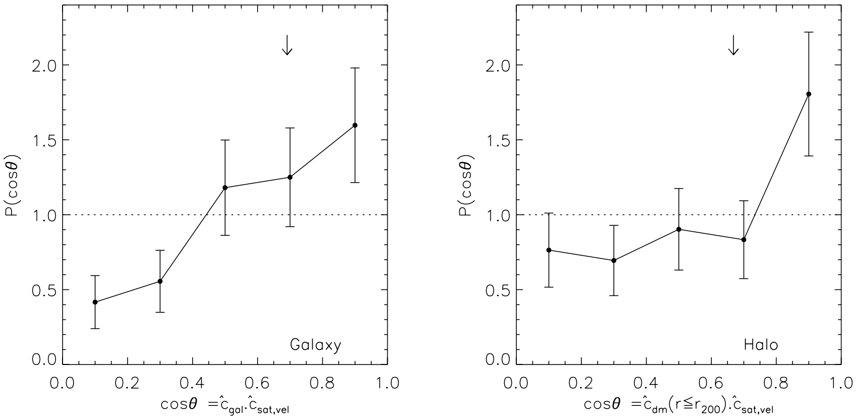

Figure 12. The alignment of the axes of the satellite velocity anisotropy with the galaxy (left-hand panel) and the dark matter halo within r_{200} (right-hand panel). The shape axes of the inner galaxy are defined within the region $r \leq 0.1r_{200}$, whilst the shape axes of the dark matter distribution are defined for $r \leq r_{200}$. The velocity dispersion of the satellites tends to be maximum in the plane perpendicular to the short axis of both the dark matter halo (right-hand panel) and the galaxy (left-hand panel).

found that the spatial orientation of the satellite galaxies at $z = 0$ is much more strongly correlated with the dark matter shape rather than the galaxy. Note that both the disc plane and short axis of the dark matter halo are defined at $z = 0$. We note that this does not take into account the evolution of the orientation of the galaxy or dark matter halo. However, our analysis does show that when satellites are accreted they have a preferential alignment relative to the dark matter halo *as defined today*.

4.5 Velocity anisotropy

By restricting attention to those systems which have 10 or more satellite galaxies, we now examine the properties of the velocity dispersion tensor. The velocity anisotropy of actual satellite galaxy populations has never been measured, but it is an important parameter for studies which use satellites as tracers of the dark matter potential. Fig. 12 shows the alignment of the principal axes of the velocity dispersion tensor with the shape axes of the galaxy and the dark matter halo.

The short axis of the velocity anisotropy tensor tends to align with the short axis of the galaxy (and the short axis of the dark matter distribution). This suggests that the velocity dispersion of the satellites tends to be maximum in the plane perpendicular to the short axis, i.e. in the plane of the disc. This cylindrical alignment of the velocity anisotropy tensor agrees with our earlier findings that there is a bias towards co-rotating satellite orbits. Note that here we have no direct comparison to the Milky Way satellites as their tangential velocity components are poorly constrained.

The anisotropy parameter, β, is defined as

$$\beta = 1 - \frac{\langle V_t^2 \rangle}{2\langle V_r^2 \rangle} = 1 - \frac{\langle V_\theta^2 \rangle + \langle V_\phi^2 \rangle}{2\langle V_r^2 \rangle}. \quad (9)$$

This is a measure of how radially or tangentially biased the satellite orbits are. To distinguish between polar and equatorial biased orbits, we define two more anisotropy parameters:

$$\beta_\theta = 1 - \frac{\langle V_\theta^2 \rangle}{\langle V_R^2 \rangle}, \quad \beta_\phi = 1 - \frac{\langle V_\phi^2 \rangle}{\langle V_R^2 \rangle}. \quad (10)$$

These quantities are defined in a cylindrical polar coordinate system (R, ϕ, z) aligned such that the z-axis is normal to the disc.

In the top left-hand panel of Fig. 13, we show the radial dependence of the radial and tangential velocity components. The solid lines are for the satellite galaxies, whilst the dashed lines are for the dark matter. Radial velocities dominate over tangential velocities at all radii for the dark matter particles. The satellite galaxies have more tangentially biased orbits in the inner regions ($r < 0.5r_{200}$) and only become radially biased at larger radii ($r > r_{200}$). Over a wide radial range, the satellites are consistent with an isotropic velocity distribution. This can also be seen in the radial dependence of β shown in the bottom left-hand panel. The two right-hand panels decompose the tangential velocity component into its polar and equatorial parts. The tangential bias of the satellite orbits in the

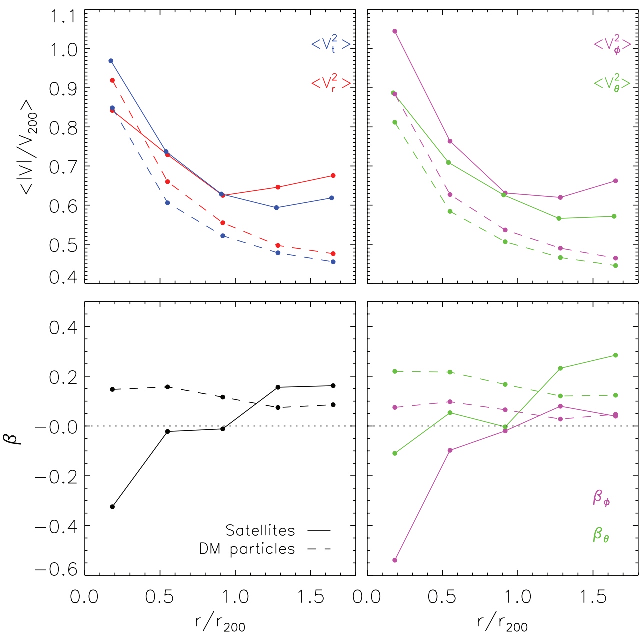

Figure 13. Top left-hand panel: the rms radial (V_r, red) and tangential (V_t, blue) velocity components as a function of radius. The solid and dashed lines are for the satellite galaxies and dark matter particles, respectively. Top right-hand panel: the rms equatorial (V_ϕ, magenta) and polar (V_θ, green) components as a function of radius. Bottom left-hand panel: the velocity anisotropy parameter (β) as a function of radius. β is consistent with isotropy over a wide radial range. Bottom right-hand panel: the polar and equatorial velocity anisotropy components (β_θ, β_ϕ) as a function of radius.

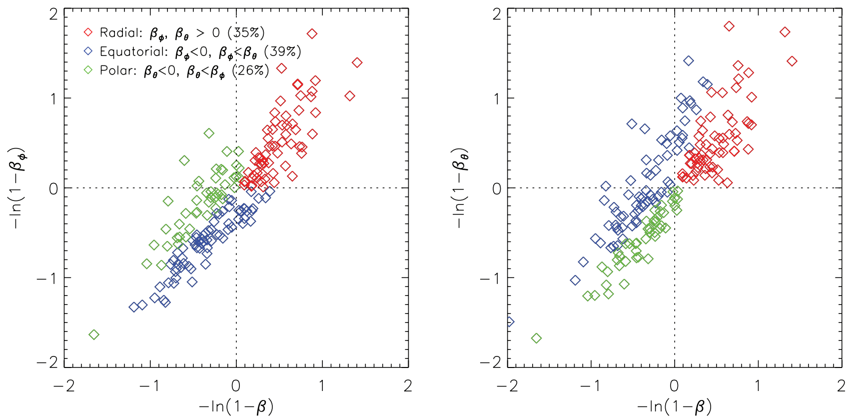

Figure 14. The polar (β_θ, right-hand panel) and equatorial (β_ϕ, left-hand panel) velocity anisotropy parameters against the overall anisotropy parameter, β. Each point represents a system of 10 or more satellites (within $2r_{200}$) belonging to an individual galaxy. Red, blue and green points represent orbits dominated by radial, equatorial and polar motions, respectively. There is significant halo-to-halo scatter in the overall velocity anisotropy.

inner regions is dominated by their equatorial motion. This is seen in the bottom right-hand panel where β_ϕ is (comparatively) large and negative at small radii. The equatorial component dominates over the polar component for the dark matter particles over the whole radial range. Dark matter haloes are dispersion supported (see Fig. 2), and the dominance of equatorial velocity components over the polar components leads to the (slight) flattening of the dark matter halo in the z-direction.[5]

In Fig. 13, we have stacked all the satellites in our sample together by normalizing radial distances by r_{200} and velocities by V_{200}. For parent haloes with 10 or more satellites within $2r_{200}$, we plot the velocity anisotropy parameters, β, β_θ and β_ϕ, in Fig. 14. It is apparent that there is a wide spread in the β parameters for individual haloes in the range $-2 < \beta < 0.8$. By stacking all the satellites of different haloes together, we find β values ranging from -0.4 to 0.2 over the same radial range. We can see from Fig. 14 that there is a slight bias towards satellite systems dominated by motion in the equatorial plane (39 per cent) but many satellite systems are dominated by their radial motions (35 per cent) or are biased towards polar orbits (26 per cent).

The velocity anisotropy parameter, β, is an important factor required to estimate the masses of Local Group galaxies such as the Milky Way and M31 (see Section 5). This parameter is difficult to observe as in most cases only line-of-sight velocities are available and we lack full 3D velocity information. To overcome this, many authors adopt anisotropy parameters derived from simulations (e.g. Xue et al. 2008; Watkins, Evans & An 2010). Our finding that there is significant halo-to-halo scatter means that significant caution is warranted when applying a velocity anisotropy applicable to a simulated satellite system of an individual halo *or* from a stacked sample of satellites to our own Milky Way Galaxy.

5 AN APPLICATION: MASS ESTIMATORS

In practice, simple estimators are often used to compute the mass of a dark halo from the positions and velocities of the satellite galaxies (e.g. Watkins et al. 2010). They depend on simplifying assumptions, such as underlying spherical symmetry of the dark halo, or constant velocity anisotropy. As we have seen, there are numerous effects present in the simulations – triaxiality of the halo, continuing infall to the present day, variation of anisotropy with radius – that are not accounted for in the mass estimators. Hence, it is interesting to see how the estimators fare against simulation data.

The projected mass estimator (PME) introduced by Bahcall & Tremaine (1981) takes the form

$$M = \frac{C_{\rm p}}{GN} \sum_{i=1}^{N} v_{{\rm los},i}^2 R_i, \qquad (11)$$

where R and $v_{\rm los}$ are the projected positions and line-of-sight velocities of the N satellite galaxies. The constant is $C_{\rm p} = 16/\pi$ (isotropic) or $C_{\rm p} = 32/\pi$ (radial orbits).

The tracer mass estimator (TME) is given in Watkins et al. (2010; see also Evans et al. 2003). It assumes a spherically symmetric power law for the halo potential $\Phi \propto r^{-\alpha}$. We use the form

$$M = \frac{C_{\rm T}}{GN} \sum_{i=1}^{N} v_{{\rm los},i}^2 R_i^\alpha, \qquad (12)$$

where $\alpha \sim 0.5$ and the constant $C_{\rm T}$ is given in equation (26) of Watkins et al. (2010) and depends on the velocity anisotropy β. In particular, $\Phi \propto r^{-0.5}$ is a good approximation to a Navarro–Frenk–White (Navarro, Frenk & White 1996, 1997) profile often used to describe simulated dark matter haloes. We assume isotropic orbits ($\beta = 0$), but investigate the validity of this assumption by comparing the estimated masses when the true velocity anisotropy of the tracer satellites is used.

Equations (11) and (12) provide an estimate for the total mass within the radius of the furthest tracer ($r_{\rm out}$). We select an arbitrary viewing angle for our simulated haloes to generate projected positions and line-of-sight velocities. We then compute the ‘true’ mass within $r_{\rm out}$ for each halo and compare to masses found via the two mass estimators. Note that we only select satellites within $r < 1.5r_{200}$. We use all satellites, but check that our results are not significantly affected when only luminous satellites are included.

In Fig. 15, we present histograms of the ratio between the estimated and true mass. We define the ‘fraction of reasonable estimates’ (FRE) as the fraction of estimates in the range $0.5 < M_{\rm est}/M_{\rm true} < 2$. We also give the interquartile range (IQR) of the mass estimates in Fig. 15. Both the TME and the PME perform

[5] Note the flattening of the dark matter halo is not always in the z-direction (defined relative to the inner disc) as there can be misalignments between the short axis of the dark matter distribution and the z-axis of the galaxy, especially at larger radii (see Section 3). However, there is reasonably good alignment for the majority of haloes.

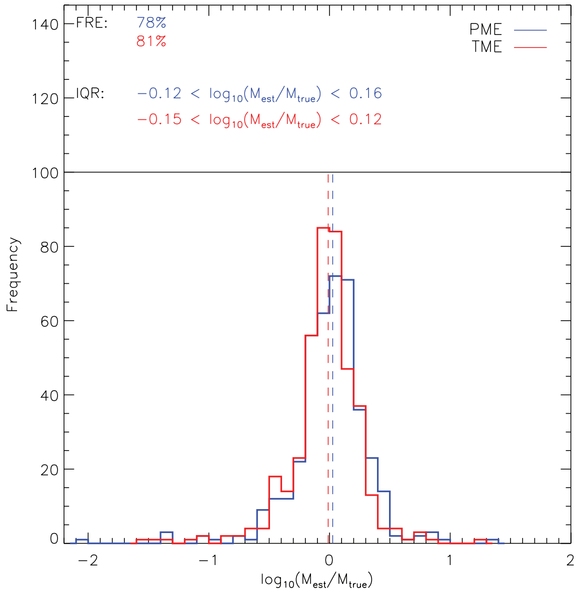

Figure 15. Histograms showing the ratio of the estimated mass to the true mass for the two different mass estimators. The PME and TME are shown by the blue and red lines, respectively. We give the FRE and the IQR as defined in the text.

well, with ≈81 and 78 per cent of the estimates satisfying our 'reasonable' criteria, respectively.[6] The TME performs slightly better than the PME (note the more symmetrical distribution in Fig. 15), but both provide good results especially considering the rather idealized assumptions under which they are derived. The IQR shows that the uncertainty in the mass estimates given by the simulations is of similar magnitude (∼30 per cent) to the statistical uncertainty found by Watkins et al. (2010) in their estimates of the Milky Way mass.

Fig. 16 illustrates how the mass given by the TME varies when we use the true velocity anisotropy parameter instead of assuming an isotropic distribution. Assuming isotropy for tangential orbits leads to an overestimate in the mass, whilst the reverse is true for radial orbits. The median absolute difference between the isotropic estimator and the true anisotropy estimator is 2 per cent $M_{\rm true}$. Unless the velocity anisotropy is strongly radial or tangential, the assumption of isotropy yields reasonable mass estimates. This is important for the application of such estimators to observational data, as we rarely have observationally derived values of the velocity anisotropy parameter.

In our samples of satellite galaxies, approximately 3 per cent are unbound. Whilst unbound satellites are not common, their inclusion in mass estimators can cause fairly large deviations from the true mass value. We compute the estimated mass with and without the unbound satellites for the 46 haloes which contain at least one unbound satellite (within $1.5r_{200}$). The left-hand panel of Fig. 17 shows the distribution of the relative difference between the mass estimates. The right-hand panel plots the two mass estimates against one another. Inclusion of unbound satellites causes a systematic overestimate of the mass. The TME and PME have median differences of 45 and 55 per cent $M_{\rm true}$ when unbound satellites are included.

[6] By restricting ourselves to systems with 10 or more satellites, the FRE increases to ∼90 per cent.

6 CONCLUSIONS

We investigated the orbital properties of the satellites of late-type galaxies using the GIMIC suite of simulations (Crain et al. 2009). These state-of-the-art simulations incorporate baryonic physics into a ΛCDM cosmological framework and produce realistic disc galaxies at $z = 0$. We analyse the phase-space distributions of the satellite galaxies relative to the luminous baryonic material (i.e. the central galaxy disc) as well as the unseen dark matter component with a large sample of galaxies. In this way we can provide a more direct comparison with observations. Our sample of parent haloes was chosen to be relaxed systems in the mass range $5 \times 10^{11} < M_{200}/{\rm M}_{\odot} < 5 \times 10^{12}$, which broadly overlaps with the mass of our own Milky Way galaxy and of M31.

The parent dark matter haloes in our sample are generally triaxial but roughly spherical and have axial ratios which are roughly constant with radius ($\langle s_{\rm dm}\rangle \sim 0.8$). Comparison to the dark matter only counterparts of our sample shows that the inclusion of baryonic physics affects the shapes of the dark matter haloes significantly, even out to r_{200}. The central galaxy (or 'disc') is often misaligned in both shape and angular momentum with the dark matter halo. The inner regions of the dark matter halo are well aligned with the central galaxy but there can be substantial misalignments at larger radii, in the region most relevant for the satellite galaxies. We find that for radii $r \sim r_{200}$, the short axis of approximately 30 per cent of our parent dark matter haloes are significantly misaligned from the short axis (or z-direction) of the inner galaxy ($\theta > 45°$). In velocity space, the net spin of the dark matter halo can be almost perpendicular to the angular momentum vector of the inner galaxy in ∼40 per cent of our sample and 2 per cent are even spinning in the opposite sense to the inner galaxy.

There is an obvious spatial bias between the dark matter of the parent halo and the satellite galaxies. The satellite system has a more flattened shape than the dark matter halo and is not as centrally concentrated. By considering all systems with 10 or more satellites within r_{200}, we find that the satellites preferentially align in a plane perpendicular to the short axis of the dark matter halo. However, owing to the misalignments between the inner galaxy and (outer) dark matter halo, this preferential alignment is much weaker relative to the inner galaxy (cf. Agustsson & Brainerd 2006). In fact, by only considering the 10 highest stellar mass satellites in each system, we find the distribution of satellites is almost uniform relative to the central disc and the 'unusual' orientation of the classical Milky Way dwarfs is not uncommon: 20 per cent of satellite systems are perpendicular (within 10°) to the disc. In a similar fashion to Brainerd (2005), we find the probability distribution of the orientation of the satellite galaxies relative to their hosts by stacking *all* of the satellites in our sample. In qualitative agreement with the observational results from SDSS and the 2dF Galaxy Redshift Survey, we find that the satellites have a weak bias towards planar alignment relative to the disc. However, there is a much stronger alignment relative to the dark matter halo shape.

It has been suggested that the Milky Way satellites may occupy a rotationally supported disc (Metz et al. 2008). We find that satellite systems which are planar and rotationally supported are relatively uncommon (∼9 per cent) in the simulations. This often occurs when a large fraction of the satellites are accreted in a group that retains its coherence in velocity space until $z = 0$. We find that it is not unusual to have three out of 10 satellites with orbital poles within 30° of the normal to their spatial configuration. This is consistent with the available proper motion data on the classical dwarfs. However,

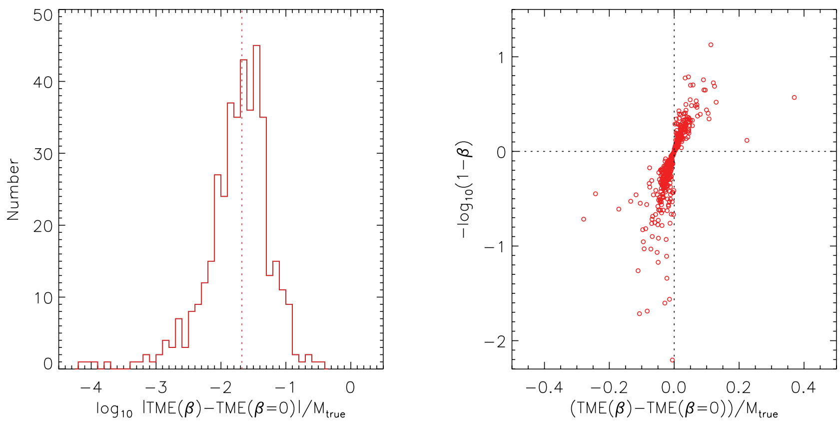

Figure 16. Left-hand panel: histogram showing the absolute difference in the estimated mass when the actual velocity anisotropy is used instead of assuming $\beta = 0$. This is normalized by the true mass. Right-hand panel: the variation in the mass estimator when the true velocity anisotropy is used as a function of velocity anisotropy.

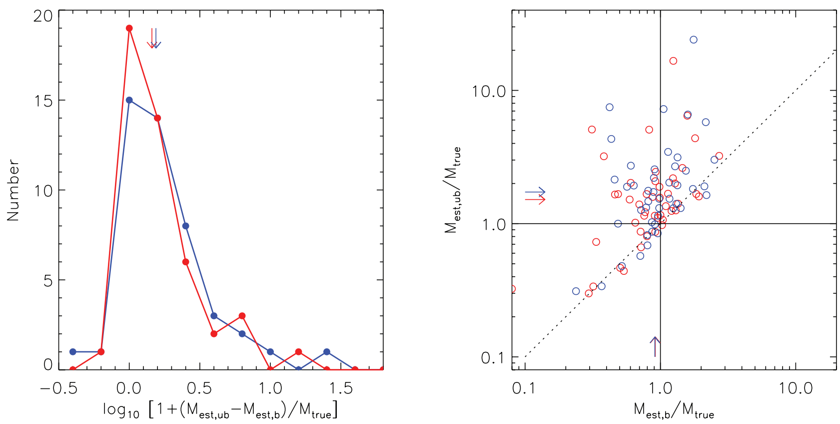

Figure 17. Left-hand panel: number distribution showing the relative difference in the mass estimates when unbound satellites are included or excluded in the analysis. Median values are shown by downward pointing arrows. Right-hand panel: the ratio between the estimated mass and true mass in the case where unbound satellites are included (*y*-axis) and when they are not (*x*-axis). The colour scheme is the same as Fig. 15. Arrows represent the median values.

we find that if a substantial number of the classical dwarfs of the Milky Way (e.g. seven out of 10) were found to have orbital poles aligned with the normal to the disc of satellites, then this would be inconsistent with the results of our simulations.

There is a bias towards co-rotating satellite orbits relative to both the angular momentum of the disc and the net spin of the dark matter halo. This is more pronounced in the inner regions of the halo. This confirms earlier results relating to dark matter only simulations (e.g. Lovell et al. 2011), but the bias with respect to the inner disc is weaker owing to the angular momentum misalignments between the inner galaxy and dark matter halo. A preference for co-rotating orbits is a natural consequence of the hierarchical assembly of galaxies whereby satellites accreted at earlier times are related to those substructures that helped spin-up the galaxy. We confirmed this by finding a stronger bias towards prograde orbits by the more massive satellites that were accreted at earlier times. By tracing back the infall orientation of our sample of satellite galaxies, we find that their anisotropic distribution is due to their preferential accretion in directions perpendicular to the short axis of the dark matter distribution. There is a weaker correlation with the orientation of the inner galaxy.

The velocity anisotropy tensor for the satellite galaxy systems is cylindrically aligned relative to the central disc. Tangential motions dominate at smaller radii, often due to the prevalence of equatorial (as opposed to polar) orbits. The velocity anisotropy, β, is an important parameter which is largely inaccessible with present observations. Here we show that β is consistent with zero over a large radial range when all satellites are stacked together. However, inspection on a halo-by-halo basis shows that there is a significant degree of scatter between haloes. This scatter puts into question the validity of using a single simulation as a template velocity anisotropy to be applied to real galaxies.

Finally, we considered an application of the orbital properties of the satellite galaxies. We tested two popular mass estimators in the literature which make use of the projected positions and line-of-sight velocities of tracers, such as satellite galaxies, to estimate the mass of the parent halo. The PME and the TME both perform well and estimate 'reasonable' (within a factor of 2 of the true mass) halo masses. The TME performs slightly better as it assumes that the satellites are tracers of the halo potential rather than having their density profile generated by the dark matter potential (as assumed by the PME). We found that an unknown velocity anisotropy parameter can lead to incorrect mass estimates but these are only substantial when β is significantly non-isotropic. In addition, the inclusion of unbound satellites can cause large overestimates of the true halo mass.

ACKNOWLEDGMENTS

AJD thanks the Science and Technology Facilities Council (STFC) for the award of a studentship, whilst VB and AF acknowledge financial support from the Royal Society. IGM is supported by a Kavli Institute Fellowship at the University of Cambridge. CSF acknowledges a Royal Society Wolfson Research Merit award. RAC is supported by the Australian Research Council via a Discovery Project grant. The simulations presented here were carried out using the HPCx facility at the Edinburgh Parallel Computing Centre (EPCC) as part of the EC's DEISA 'Extreme Computing Initiative', the Cosmology Machine at the Institute for Computational Cosmology of Durham University and on the HPC Cluster Darwin at the University of Cambridge. We wish to thank Joop Schaye and Volker Springel for help and advice.

REFERENCES

Abadi M. G., Navarro J. F., Fardal M., Babul A., Steinmetz M., 2010, MNRAS, 407, 435
Agertz O., Teyssier R., Moore B., 2009, MNRAS, 397, L64
Agustsson I., Brainerd T. G., 2006, ApJ, 650, 550
Agustsson I., Brainerd T. G., 2010, ApJ, 709, 1321
Azzaro M., Zentner A. R., Prada F., Klypin A. A., 2006, ApJ, 645, 228
Bahcall J. N., Tremaine S., 1981, ApJ, 244, 805
Bailin J., Steinmetz M., 2005, ApJ, 627, 647
Bailin J. et al., 2005, ApJ, 627, L17
Baugh C. M., 2006, Rep. Progress Phys., 69, 3101
Bett P., Eke V., Frenk C. S., Jenkins A., Okamoto T., 2010, MNRAS, 404, 1137
Brainerd T. G., 2005, ApJ, 628, L101
Cole S., Aragon-Salamanca A., Frenk C. S., Navarro J. F., Zepf S. E., 1994, MNRAS, 271, 781
Crain R. A. et al., 2009, MNRAS, 399, 1773
Crain R. A., McCarthy I. G., Frenk C. S., Theuns T., Schaye J., 2010, MNRAS, 407, 1403
Dalla Vecchia C., Schaye J., 2008, MNRAS, 387, 1431
Deason A. J., Belokurov V., Evans N. W., 2011, MNRAS, 411, 1480
Dolag K., Borgani S., Murante G., Springel V., 2009, MNRAS, 399, 497
Dubinski J., 1994, ApJ, 431, 617
Dubinski J., Carlberg R. G., 1991, ApJ, 378, 496
Duffy A. R., Schaye J., Kay S. T., Dalla Vecchia C., Battye R. A., Booth C. M., 2010, MNRAS, 405, 2161
Einasto J., Haud U., 1989, A&A, 223, 89
Evans N. W., Wilkinson M. I., Perett K. M., Bridgas T. J., 2003, ApJ, 583, 752
Fall S. M., Efstathiou G., 1980, MNRAS, 193, 189
Fellhauer M. et al., 2006, ApJ, 651, 167
Font A., McCarthy I. G., Crain R. A., Theuns T., Schaye J., Wiersma R. P. C., Della Vecchia C., 2011, MNRAS, submitted (arXiv:1102.2526)
Franx M., Illingworth G., de Zeeuw T., 1991, ApJ, 383, 112
Frenk C. S., White S. D. M., Davis M., Efstathiou G., 1988, ApJ, 327, 507
Gao L., Navarro J. F., Cole S., Frenk C. S., White S. D. M., Springel V., Jenkins A., Neto A. F., 2008, MNRAS, 387, 536
Geehan J. J., Fardal M. A., Babul A., Guhathakurta P., 2006, MNRAS, 366, 996
Gnedin O. Y., Kravtsov A. V., Klypin A. A., Nagai D., 2004, ApJ, 616, 16
Governato F., Willman B., Mayer L., Brooks A., Stinson G., Valenzuela O., Wadsley J., Quinn T., 2007, MNRAS, 374, 1479
Guo Q., White S., Li C., Boylan-Kolchin M., 2010, MNRAS, 404, 1111
Haardt F., Madau P., 2001, in Neumann D. M., Tran J. T. V., eds, Clusters of Galaxies and the High Redshift Universe Observed in X-rays. Editions Frontieres, Paris, p. 64
Hammer F., Puech M., Chemin L., Flores H., Lehnert M. D., 2007, ApJ, 662, 322
Heavens A., Peacock J., 1988, MNRAS, 232, 339
Helmi A., 2004, MNRAS, 351, 643
Heymans C., White M., Heavens A., Vale C., van Waerbeke L., 2006, MNRAS, 371, 750
Hoekstra H., Yee H. K. C., Gladders M. D., 2004, ApJ, 606, 67
Holmberg E., 1969, Arkiv Astron., 5, 305
Hwang H. S., Park C., 2010, ApJ, 720, 522
Ibata R., Irwin M., Lewis G. F., Stolte A., 2001, ApJ, 547, L133
Johnston K. V., Law D. R., Majewski S. R., 2005, ApJ, 619, 800
Kang X., Mao S., Gao L., Jing Y. P., 2005, A&A, 437, 383
Kazantzidis S., Kravtsov A. V., Zentner A. R., Allgood B., Nagai D., Moore B., 2004, ApJ, 611, L73
Kennicutt R. C., Jr, 1998, ApJ, 498, 541
Kroupa P., Theis C., Boily C. M., 2005, A&A, 431, 517
Law D. R., Majewski S. R., 2010, ApJ, 714, 229
Li Y., Helmi A., 2008, MNRAS, 385, 1365
Libeskind N. I., Frenk C. S., Cole S., Helly J. C., Jenkins A., Navarro J. F., Power C., 2005, MNRAS, 363, 146
Libeskind N. I., Cole S., Frenk C. S., Okamoto T., Jenkins A., 2007, MNRAS, 374, 16
Libeskind N. I., Frenk C. S., Cole S., Jenkins A., Helly J. C., 2009, MNRAS, 399, 550
Libeskind N. I., Yepes G., Knebe A., Gottlöber S., Hoffman Y., Knollmann S. R., 2010, MNRAS, 401, 1889
Lovell M., Eke V., Frenk C., Jenkins A., 2011, MNRAS, 413, 3013
Ludlow A. D., Navarro J. F., Springel V., Jenkins A., Frenk C. S., Helmi A., 2009, ApJ, 692, 931
Lynden Bell D., 1976, MNRAS, 174, 695
Lynden Bell D., Lynden Bell R. M., 1995, MNRAS, 275, 429
Macciò A. V., Moore B., Stadel J., Diemand J., 2006, MNRAS, 366, 1529
Mandelbaum R., Hirata C. M., Broderick T., Seljak U., Brinkmann J., 2006, MNRAS, 370, 1008
Metz M., Kroupa P., Libeskind N. I., 2008, ApJ, 680, 287
Metz M., Kroupa P., Theis C., Hensler G., Jerjen H., 2009, ApJ, 697, 269
Navarro J. F., Frenk C. S., White S. D. M., 1996, ApJ, 462, 563
Navarro J. F., Frenk C. S., White S. D. M., 1997, ApJ, 490, 493
Navarro J. F. et al., 2004, MNRAS, 349, 1039
Neto A. F. et al., 2007, MNRAS, 381, 1450
Olling R. P., Merrifield M. R., 2000, MNRAS, 311, 361
Parker L. C., Hoekstra H., Hudson M. J., van Waerbeke L., Mellier Y., 2007, ApJ, 669, 21
Sales L., Lambas D. G., 2004, MNRAS, 348, 1236
Sales L. V., Navarro J. F., Lambas D. G., White S. D. M., Croton D. J., 2007, MNRAS, 382, 1901
Schaye J., Dalla Vecchia C., 2008, MNRAS, 383, 1210
Schaye J. et al., 2010, MNRAS, 402, 1536
Shaw L. D., Weller J., Ostriker J. P., Bode P., 2006, ApJ, 646, 815
Smith M. C. et al., 2009, MNRAS, 399, 1223
Somerville R. S., Primack J. R., 1999, MNRAS, 310, 1087
Springel V., 2005, MNRAS, 364, 1105
Springel V., White S. D. M., Tormen G., Kauffmann G., 2001, MNRAS, 328, 726
Springel V. et al., 2005, Nat, 435, 629
Thomas P. A., Muanwong O., Pearce F. R., Couchman H. M. P., Edge A. C., Jenkins A., Onuora L., 2001, MNRAS, 324, 450
Tully R. B. et al., 2006, AJ, 132, 729
Vitvitska M., Klypin A. A., Kravtsov A. V., Wechsler R. H., Primack J. R., Bullock J. S., 2002, ApJ, 581, 799
Warnick K., Knebe A., 2006, MNRAS, 369, 1253
Watkins L. L., Evans N. W., An J. H., 2010, MNRAS, 406, 264
White S. D. M., 1984, ApJ, 286, 38
White S. D. M., Frenk C. S., 1991, ApJ, 379, 52
Widrow L. M., Perrett K. M., Suyu S. H., 2003, ApJ, 588, 311
Wiersma R. P. C., Schaye J., Smith B. D., 2009a, MNRAS, 393, 99
Wiersma R. P. C., Schaye J., Theuns T., Dalla Vecchia C., Tornatore L., 2009b, MNRAS, 399, 574
Xue X. X. et al., 2008, ApJ, 684, 1143
Yang X., van den Bosch F. C., Mo H. J., Mao S., Kang X., Weinmann S. M., Guo Y., Jing Y. P., 2006, MNRAS, 369, 1293

Zaritsky D., Smith R., Frenk C. S., White S. D. M., 1997, ApJ, 478, L53
Zentner A. R., Kravtsov A. V., Gnedin O. Y., Klypin A. A., 2005, ApJ, 629, 219

APPENDIX A: CONVERGENCE TESTS

Our sample of simulated galaxies is drawn from the five intermediate-resolution GIMIC simulations, which have been run to $z = 0$. In addition, there is one higher resolution GIMIC simulation (the -2σ region) available to $z = 0$. This simulation has eight times better resolution and allows us to assess the numerical convergence of our results. We have checked that the main results in this paper are unchanged in this higher resolution GIMIC simulation. Here, we give examples for two of our main results.

In Fig. A1, we show the distributions of misalignments between the galaxy and dark matter halo short axes both for $r \leq 0.1r_{200}$ (left-hand panel) and for $r \leq r_{200}$ (right-hand panel) for the high-resolution GIMIC runs. This is shown in the bottom panels of Fig. 3 in the main text. There is very good agreement between the high- and intermediate-resolution simulations. Our finding in the main text that there can be significant misalignments between the galaxy and the outer dark matter halo is therefore robust to an increase in resolution.

In Fig. A2, we show the distribution of alignments between the short axes of the satellite systems and the short axes of the dark matter halo (for $r \leq r_{200}$) and the galaxy of their parent haloes (see Fig. 6 in the main text). We only consider the 10 brightest satellites within r_{200}. The black and blue lines show the distributions in the intermediate- and high-resolution simulations, respectively. Note that only the -2σ volume is available at $z = 0$ in the high-resolution simulations, so we do not achieve the same statistics as the intermediate-resolutions runs. Approximately 30 parent haloes have 10 or more satellites within r_{200} in the high-resolution sample (cf. ~80 in the intermediate-resolution sample). For both the intermediate- and high-resolution runs, the satellite distribution preferentially aligns in a plane perpendicular to the short axis of the dark matter distribution and the satellites show no preferential alignment relative to the galaxy. Thus, our conclusions from Fig. 6 in the main text are robust to an increased resolution.

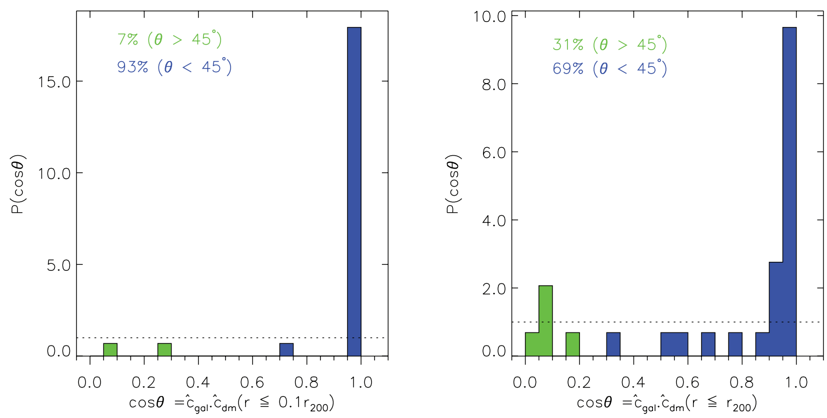

Figure A1. The distribution of misalignment angles between the short axis of the galaxy and the short axis of the dark matter halo for $r \leq 0.1r_{200}$ (left-hand panel) and $r \leq r_{200}$ (right-hand panel), respectively. This is for the high-resolution GIMIC simulations (cf. Fig. 3 for the intermediate-resolution version of this plot).

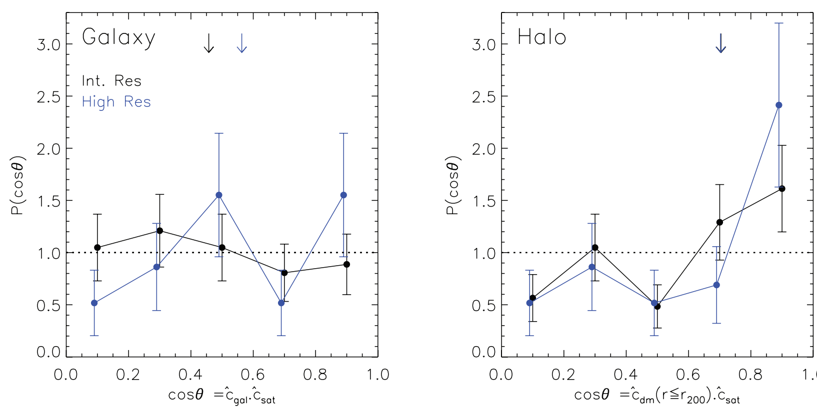

Figure A2. The orientation of the short axes of the satellite distribution relative to the short axes of the parent galaxy and dark matter halo (defined within r_{200}). The 10 brightest satellites within r_{200} are used to compute the shapes of the satellite distribution. Downward pointing arrows denote the median of the distributions and the dotted lines indicate a uniform distribution. The error bars denote Poisson uncertainties. The black and blue lines show the distributions in the intermediate- and high-resolution simulations, respectively.

This paper has been typeset from a TEX/LATEX file prepared by the author.